Quaternary Science Reviews
April 2024, Volume 329 Pages 108564 (15p.)
https://doi.org/10.1016/j.quascirev.2024.108564
https://archimer.ifremer.fr/doc/00881/99274/

A new insight of the MIS 3 Dansgaard-Oeschger climate oscillations in western Europe from the study of a Belgium isotopically equilibrated speleothem

Peral Marion [1, 2, *], Marchegiano Marta [1, 3], Verheyden Sophie [4], Goderis Steven [1], Van Helden Tom [5], Vanhaecke Frank [5], Van Acker Thibaut [5], Jia Xue [6], Cheng Hai [6], Fiebig Jens [7], Fourcade Tiffanie [2, 8], Snoeck Christophe [1], Claeys Philippe [1]

[1] Archaeology, Environmental Changes & Geo-Chemstry, Vrije Universiteit Brussel, Belgium
[2] Environnements et Paléoenvironnements Océaniques et Continentaux (EPOC), UMR CNRS 5805, Université de Bordeaux, 33600 Pessac, France
[3] Departamento de Estratigrafía y Paleontología, Universidad de Granada, 18071 Granada, Spain
[4] Royal Belgian Institute for Natural Sciences (RBINS), Belgium
[5] Atomic & Mass Spectrometry – A&MS Research Group, Department of Chemistry, Ghent University, Campus Sterre, Krijgslaan 281-S12, 9000 Ghent, Belgium
[6] Institute of Global Environmental Change, Xi'an Jiaotong University, China
[7] Institut für Geowissenschaften, Goethe Universität, Altenhöferallee 1, 60438 Frankfurt am Main, Germany
[8] Archéosciences Bordeaux, UMR 6034, Université Bordeaux Montaigne, CNRS, Maison de l'Archéologie, Esplanade des Antilles, 33600 Pessac, France

* Corresponding author : Marion Peral, email address : marion.peral@u-bordeaux.fr

Abstract :

The Marine Isotope Stage (MIS) 3 records abrupt transitions from cold stadial to temperate interstadial climate conditions, termed Dansgaard-Oeschger (DO) events. Reconstructing these rapid climate changes is crucial for documenting the prevailing climatic conditions in Europe during the extinction of the Neanderthals. However, only few continental records are available to define the continental climatic responses to DO changes. Here, the elemental and stable isotope compositions of a well-dated speleothem in Belgium covering the MIS 3 are documented. This speleothem precipitated under equilibrium conditions based on Δ48 thermometry, allowing the use of Δ47 thermometry with confidence. Moreover, the precision and accuracy of our clumped-isotope analyses are demonstrated through the long-term monitoring of international Δ47 standards. The acquired unique thermometry paleoclimatic dataset enables the reconstruction of temperature based on the hydrological information (oxygen-18 of drip water; δ18Ow) and sheds new light on the DO climate variations. A temperature differential of ~7 °C is associated with alternating temperate warm and wet Interstadials to cold and dry stadials. The DO-12 is the most pronounced MIS 3 interstadial in the record and appears to be marked by a delay of 1000 years between climate enhancement (warmer temperature) and water availability (moisture increase). By combining our speleothem record with other continental and marine archive, the spatial variability of DO changes in Europe during the MIS 3 is defined. A gradual climate deterioration with colder and drier conditions, associated with the Heinrich 4 event, progressed southwards through Europe. This spatial climatic degradation, during the last phase of Neanderthal populations occupation in Europe, provides better environmental constraints for human mobility models.

Highlights

► We study an isotopically equilibrated speleothem covering the MIS 3 in Western Europe. ► A temperature differential of ~7 °C is associated with alternating interstadials to stadials. ► DO-12, the most pronounced interstadial, start with a 1000-years delay between climate enhancement and water availability. ► A southward gradual climate deterioration with colder and drier conditions is observed through western Europe. ► As no comparable southward Neanderthal decline is observed, a climatic role in the Neanderthals' extinction may be excluded.

1. INTRODUCTION

The Marine Isotope Stage 3 (MIS 3) – a period between 57 and 27 ka ago during the Last Glacial (Lisiecki and Raymo, 2005) – is associated with several abrupt climatic warming phases known as Dansgaard-Oeschger (DO) events. Registered in Greenland ice core oxygen isotope ratio records (Johnsen et al., 1992; Dansgaard et al., 1993; Svensson et al., 2008), these events are characterized by abrupt changes from cold (stadial climate conditions, noted GS for Greenland Stadial) to mild (interstadial climate conditions, noted GI for Greenland Interstadial), eventually followed by a return to stadial conditions (Dansgaard et al., 1993). Temperature reconstructions from Greenland ice cores suggest a rise of mean annual surface air temperature of around 15°C in only a few decades (Severinghaus et al., 1998; Huber et al., 2006; Kindler et al., 2014). A total of 11 MIS 3 DO-events have been identified, based on the GICC05 timescale (DO 5 to 15, Rasmussen et al., 2014). Within certain stadials, massive ice surges from the Laurentide Ice Sheet flushed into the North Atlantic Ocean, during so-called Heinrich events (HEs, Heinrich, 1988), as highlighted by the presence of ice-rafted debris (IRD) layers found in North Atlantic sediments (Heinrich, 1988). This freshwater input slows down the formation of North-Atlantic deep-water (Böhm et al., 2015). The HEs 3 to 5 are recorded in the MIS 3 section of Greenland ice cores and North Atlantic sediment cores, corresponding to cold phases with a typical duration of a few thousand years (Bond et al., 1993; Cacho et al., 1999; Sánchez Goñi et al., 2002). Therefore, these DO events and HEs correlate with rapid climatic changes in the circum-North Atlantic region (Bond et al., 1993; van Kreveld et al., 2000; Hemming, 2004; Rasmussen and Thomsen, 2004) and European continent (Genty et al., 2003, 2005, 2010; Wainer et al., 2009; Pons-Branchu et al., 2010; Fankhauser et al., 2016; Weber et al., 2018) with warm and wet episodes during GI and cold and dry during GS.

The MIS 3 is also characterized by the disappearance of Neanderthals, at ~41 - 39 ka in western Europe (Higham et al., 2014). Several hypotheses have been invoked to explain the Neanderthals disappearance. Recent updated archaeological synthesis shows that the onset of the *Homo sapiens* occupation of western Europe likely preceded the extinction of Neandertals (Talamo et al., 2020; Fourcade et al., 2022; Rios-Garaizar et al., 2022; Djakovic et al., 2022). This overlap may have led to competitive exclusion (Banks et al., 2008), assimilation (Smith et al., 2005) or demographic weakness (Degioanni et al., 2019). An alternative hypothesis to Neanderthal decline is abrupt changes in climate and vegetation (Staubwasser et al., 2018). The proposed mechanisms may vary regionally and temporally and could have taken place contemporaneously. However, recent simulations suggest only a regional role of rapid climate change in the European Neanderthal extinction, specifically in its western parts (Timmermann, 2020). Furthermore, the Mediterranean area (Italy) seems to record stable environmental (rainfall and vegetated soils) conditions during this period (e.g., Columbu et al., 2020). This could agree with a less strong influence of the rapid DO events in southern Europe. Unfortunately, only a few MIS 3 continental archives (Genty et al., 2003, 2005, 2010; Wainer et al., 2009; Pons-Branchu et al., 2010; Stoll et al., 2013; Sirocko et al., 2016; Weber et al., 2018) are available in western Europe. Therefore, more records are needed to better constrain the spatial climate variability in Europe during the MIS 3 and its potential influence on the Neanderthals.

Speleothems, one of the most suitable terrestrial archive, do not grow extensively during the MIS 3 in Northern Europe. The majority of MIS 3 speleothem records originate from the Alpine region (Spötl and Mangini, 2002; Spötl et al., 2006; Holzkämper et al., 2005; Moseley et al., 2014, 2020; Luetscher et al., 2015), where the basement of glaciers provides continuous meltwater enabling speleothem growth despite cold surface conditions (Spötl and Mangini, 2002). Other European speleothems grow during the warm and wet interstadials (Genty et al., 2003, 2005, 2010; Wainer et al., 2009; Pons-Branchu et al., 2010; Fankhauser et al., 2016; Weber et al., 2018) but generally stop growing during cold stadial climates (Genty et al., 2003, 2005, 2010; Wainer et al., 2009; Pons-Branchu et al., 2010; Fankhauser et al., 2016; Weber et al., 2018) due to the reduced temperature and decrease in available moisture (Wainer et al., 2009; Moseley et al., 2020).

Multi-method approaches disentangle the variety of effects and processes that control the geochemical proxy-signals. Oxygen isotope variations in carbonate (δ^{18}Oc) record both temperature and the isotopic composition of the water in which the carbonate formed (δ^{18}Ow), associated with the amount of rainfall, regional circulation system and/or through cave-specific processes, transferring the climatic signatures (McDermott, 2004; McDermott et al., 2011; Tremaine et al., 2011; Lachniet, 2009). The carbon isotope values (δ^{13}C) indicate changes in vegetation or vegetational activity (Genty et al., 2003; Tremaine et al., 2011). Because of the difficulty in interpreting the complex δ^{18}O and δ^{13}C variability, mainly due to the contribution of multiple physical and climatic processes, trace element records often provide complementary paleoclimate reconstructions. Trace element records follow changes in paleo-recharge processes in karst systems (Fairchild et al., 2001; McDermott, 2004) related to water availability (magnesium [Mg], barium [Ba], and strontium [Sr] concentrations) and to vegetation conditions above the cave (Fairchild et al., 2001; Huang et al., 2001; Treble et al., 2003; Borsato et al., 2007, phosphorous [P] concentrations). However, absolute temperature values remain necessary to constrain quantitative interpretations. The classic approach is to measure the hydrogen and oxygen isotope ratios of fluid inclusions, provided they contain sufficient water. The carbonate clumped-isotope method (Δ_{47}) constitutes an alternative thermometer, independent of the $\delta^{18}O_w$. However, kinetic effects often affect speleothems leading to isotopic disequilibrium and overestimated temperatures (Affek et al, 2008, 2014; Daëron et al., 2011; Kluge et al., 2013; Matthews et al., 2021; Nehme et al., 2023). Nevertheless, speleothems that precipitate close to isotopic equilibrium retain the original clumped isotope signal, allowing precise reconstruction of paleo-temperature variations in caves (Daëron et al., 2019). Measurement of dual-clumped isotopes (Δ_{48} alongside Δ_{47}; Fiebig et al., 2021) allows to trace potential kinetic effects and to determine whether a speleothem has precipitated in near-isotopic equilibrium (Bajnai et al., 2020).

Here, we present the first geochemical study of a Belgium flowstone speleothem (named “*Incomparable*”; taken in the Vervietois gallery in the Han-sur-Lesse cave) that documents the climatic conditions during the Early MIS 3, and advances knowledge of continental MIS 3 climate. Chronologically well constrained based on U-Th ages, the speleothem is investigated using a multi-proxy approach based on δ^{13}C and δ^{18}O analysis and trace element concentration time-series. Due to insufficient water contents in fluid inclusions, absolute Δ_{47}-derived temperatures are obtained and used to estimate the δ^{18}Ow from which the speleothem precipitated. Δ_{48} measurement is also performed to ensure that the speleothem precipitated near isotopic equilibrium. This study constitutes a unique paleoclimatologic application of clumped isotope thermometry in a speleothem precipitated close to the isotopic equilibrium, allowing the quantification of the first absolute temperatures across the MIS 3 in western Europe. Finally, our data are compared with available climatic records and the current archeological chronology of the last Neanderthal occupation in Europe to document the potential effect of climate on the Neanderthal demise.

2. SITE STUDY AND GEOLOGICAL SETTINGS

The Incomparable sample is a calcite core taken from a speleothem flowstone from the Vervietois gallery in the Han-sur-Lesse cave (Fig. 1.a&b), the largest known subterranean karstic network in Belgium, with a total length of ~ 10 km. It is located within the Calestienne, a SW–NE trending limestone belt of Middle Devonian age (50.121°N; -5.192°E WGS184). The cave system is the result of a meander cutoff of the Lesse River within the Massif de Boine, which is part of an anticline structure consisting of Middle to Late Givetian reefal limestones (Quinif, 2006). The thickness of the limestone host rock above the cave system is estimated to be around 40–70 m (Quinif, 2006). The cave is located ca. 200 km inland at an elevation of 200 m above sea level. Following the Köppen-Geiger classification (Peel et al., 2007), the climate in southern Belgium is maritime with cool summers and mild winters. For the period 1991–2020, the mean annual continental temperature was 10.0 °C with an average yearly rainfall of 855 mm at the Rochefort meteorological station, located approximately 10 km from the cave site. This rainfall is spread across the entire year with no distinct seasonal distribution (Royal Meteorological Institute, RMI). The current mean $\delta^{18}O$ value of drip water, sampled once a month in the Salle du Dôme (Fig. 1c) from August 2016 to July 2018, is -7.4 ‰ ± 0.1 ‰ (1SE), in agreement with previously published $\delta^{18}O$ values for drip water of -7.6 ‰ in the Han-sur-Lesse cave (Van Rampelbergh et al., 2014) and of -7.5 ‰ in the Père Noël cave, a nearby cave from the same cave system (Verheyden et al., 2008). The air temperature (June 2021-July 2022), at the entrance of the Verviétois gallery where the core was taken (at the Mystérieuses; Fig. 1.c) varied from 9.5 to 10.8°C, with a mean annual value of 10.2°C (Fig. 1.d). These temperatures were recorded using a home-made temperature logger 'Niphargus', Burlet et al., 2015).

The Han-sur-Lesse Cave system has been intensively studied during the last decades, making it the best understood cave system in Belgium. These studies included speleothem date and pollen analysis (Quinif and Bastin, 1994; Quinif, 2006), detailed hydrographic studies (Bonniver, 2011) and extended cave monitoring surveys (Genty and Deflandre, 1998; Poulain et al., 2015; Verheyden et al., 2008; Van Rampelbergh et al., 2014), leading to successful paleoclimate reconstructions down to the seasonal scale via speleothem analysis (Verheyden et al., 2000, 2006; 2012, 2014; Van Rampelbergh et al., 2015; Allan et al., 2018; Vansteenberge et al., 2019, 2020).

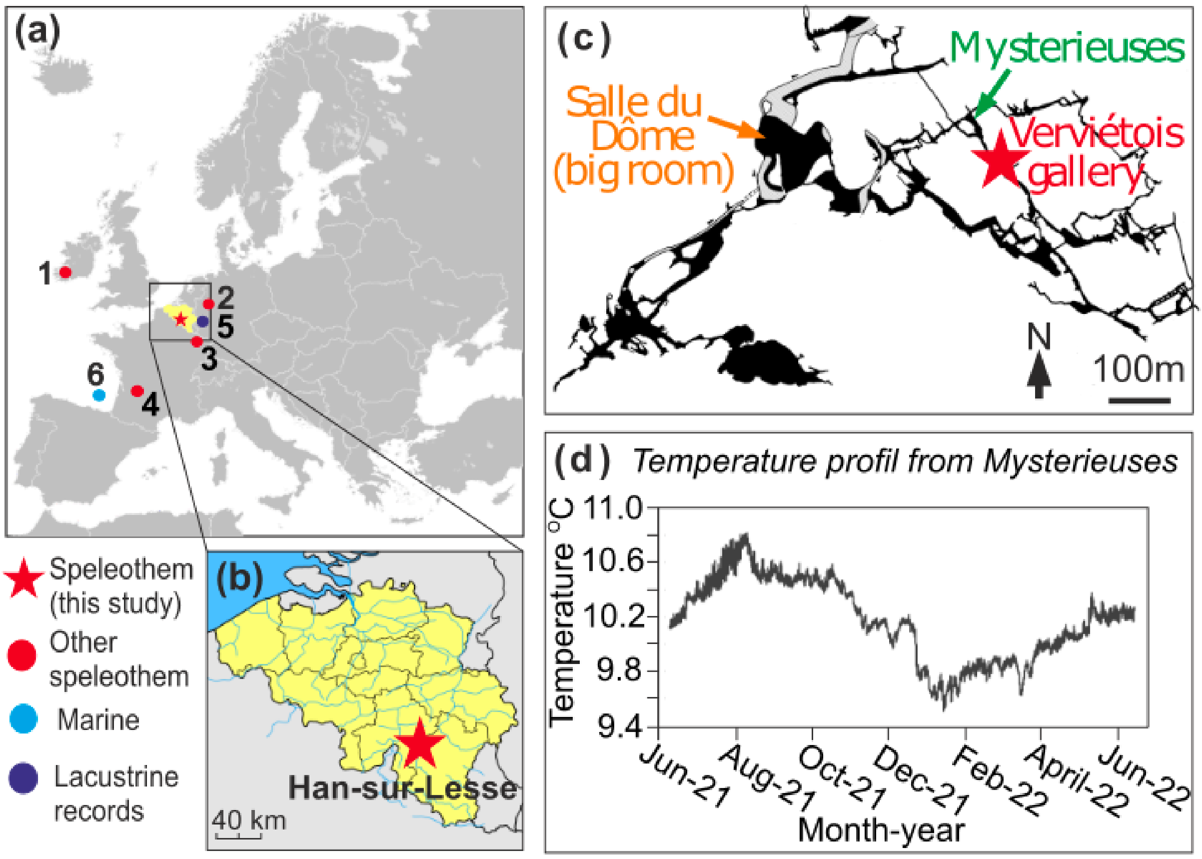

Figure 1: **Site map and modern temperature profile.** (a) European map with the locations of the speleothem studied here as well as of other speleothem archives (1. Fankhauser et al., 2016; 2. Weber et al., 2018; 3. Pons-Branchu et al., 2010; 4. Genty et al., 2003, 2010; Wainer et al., 2009), lacustrine archives (5. Sirocko et al., 2016) and marine archives (6. Sánchez-Goñi et al., 2008), (b) location of Han-sur-Lesse within Belgium, (c) Han-sur-Lesse cave with location of the Incomparable speleothem in the Verviétois gallery, the Mysterieuses gallery and the Salle du Dôme (big room) (after Quinif, 2017) and (d) a temperature profile over one year at the entrance of the Verviétois gallery in the Mystérieuses gallery.

3. ARCHEOLOGICAL CONTEXT IN WESTERN EUROPE

In the south western Europe, the Neanderthals are associated with the Châtelperronian culture (south of France, Cantabria [north Spain] and Catalonia [northeastern Spain], *e.g.* D'Errico et al., 2003; Dayet et al., 2014; Ruebens et al., 2015). No consensus on the attribution of the Châtelperronian to Neanderthals or anatomically modern humans (*e.g.* Hublin et al., 1996; Higham et al., 2010; Gravina et al., 2018; Gicqueau et al., 2023). However, we consider, in this article, that the Châtelperronian is attributed to Neanderthals because studies on the paleoproteomic technique suggest evidence for Neanderthal craftsman (Welker et al., 2016), and the only human remains dated within the Châtelperronian time range have Neandertal characters (Hublin et al., 2012; Balzeau et al., 2020; Guérin et al., 2023; Gicqueau et al., 2023).

In north-western Europe, Neanderthal occupation is less well-documented. Belgium has been repopulated by Neanderthals at the onset of MIS 3 (Romagnoli et al., 2022). Their last settlements in the region are estimated between 44 and 42 ka (Deviese et al., 2021; Abrams, 2023), while first occupation clearly attributed to Anatomically Modern Humans could have taken place later, around 42-40 kyrs (Abrams et al., 2024). As these dates are based on individual remains, further evidence may be required to compare the Neanderthal occupation based on the archeological units associated with “cultural” manifestations. The Lincombien-Ranisien-Jerzmanowicien (LRJ) culture was developed from Poland to England, and is dated between ca. 44 and 41 ka (Picin et al., 2022). However, this culture is not clearly identified anthropologically (Semal et al., 2009; Flas et al., 2011; Demidenko et al., 2023). Despite the intense ongoing debates on the attribution of LRJ, rare records from northern France place the end of the Late Middle Palaeolithic (Neanderthals occupations) around 40 ka (Locht et al., 2016; Locht, 2019), confirming the dates from Devièse et al. (2021) and Abrams (2023) as the timing of last occupation of Neanderthals in northwest Europe.

4. MATERIAL AND METHODS

4.1. *Sample preparation*

The flowstone core was cut vertically into two segments. One part was used for the analyses, while the other was kept as archive. The speleothem is 85 cm long and is divided in 4 parts (I-A, -B, -C and -D; Fig. 2.A). Each part was cut in slices of 1 cm thick. This study only focuses on the second part, labelled I-B, from 17.6 to 37.4 cm, and in particularly on the I-B2 facies (Fig. 2.A).

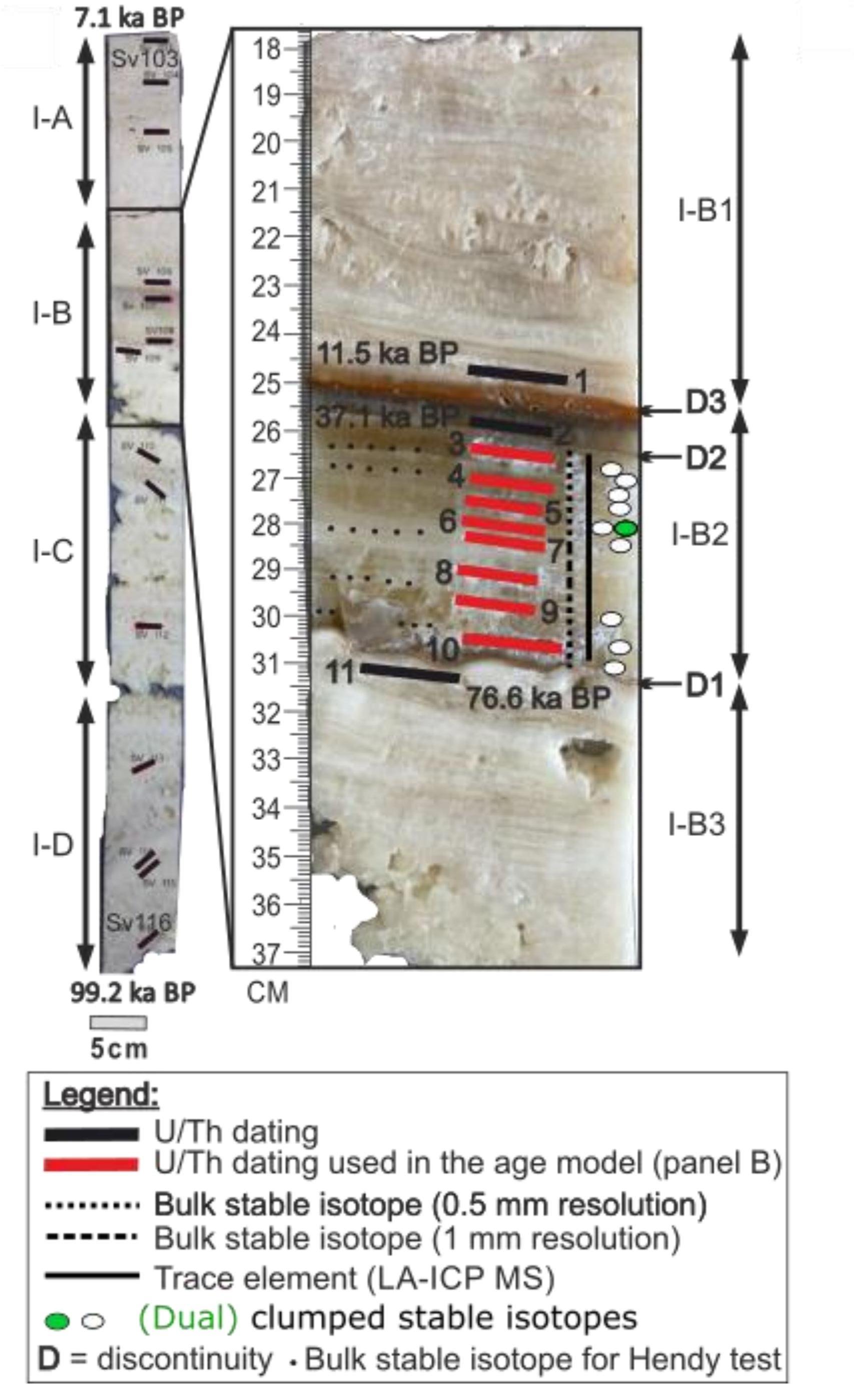

Figure 2: **Speleothem description and methodological sampling location**. Photographs of the entire Incomparable speleothem with a blow-up of the (I-B) part of the speleothem studied (I-B2). The sampling locations for each of the methods used as highlighted in this article are also indicated. The discontinuities are noted D. The intervals used for constructing the age model of the part studied (I-B2) are marked in red. The sample locations used for the U/Th dating are numbered corresponding to the dating listed in Table S1.

4.2. *$^{230}Th/^{238}U$ dating*

A total of 11 calcite samples, 9 samples of which from within the I-B2 section (Fig. 2.A) and each equivalent to ~ 300 mg were drilled for U–Th dating using a manual microdrill with a diamond drill bit. The analyses were performed on a Thermo-Scientific Neptune *Plus* multi-collector inductively coupled plasma mass spectrometer (MC-ICP-MS) at the Isotope Laboratory at Xi'an Jiaotong University. A full description with more details of the U-series methodology, on the applied chemical procedures, instrumentation, standardization, and half-lives, is available in Edwards et al. (1987), Shen et al. (2012) and Cheng et al. (2013). The uncertainties on uranium and thorium isotope ratio data were calculated offline at the 2σ level, including corrections for blanks, multiplier dark noise, abundance sensitivity and contents of the same nuclides in the spike solution. The ^{230}Th were corrected assuming an initial ^{230}Th/^{232}Th atomic ratio of $4.4 \pm 2.2 \times 10^{-6}$, the values for material at secular equilibrium with a bulk earth ^{232}Th/^{238}U values of 3.8 (Edwards et al., 2003). Ages are presented in years before 1950 CE. The age model was constructed using StalAge code (Scholz and Hoffmann 2011). Dates are available in supplementary material Table S1.

4.3. *Bulk stable isotopic analysis of calcite*

Stable carbon and oxygen isotope ratio values (δ^{13}C and δ^{18}Oc) were obtained at the Vrije University Brussel (VUB), Brussels, Belgium. In total, 104 samples were drilled using a Merchantek video controlled MicroMill device with a spatial resolution between 500 µm and 1 mm (Fig. 1.A). The speleothem surface and drill bit were cleaned with methanol before sampling. The δ^{13}C and δ^{18}O analyses were performed using a Nu-carb carbonate sample preparation system combined with a Nu-Perspective-isotope ratio mass spectrometer (IRMS). Two international standards (IAEA-603 and IAEA-CO8) were analyzed with each series of samples. Analytical precision for the δ^{13}C and δ^{18}O measurements is better than 0.05 ‰ for δ^{13}C and 0.1 ‰ for δ^{18}O (both at the 1SD level). The quality of the measurements is ensured by analyzing an in-house Carrara marble standard and an international reference material NBS-18. All δ^{13}C and δ^{18}O values are reported relative to V-PDB. Samples are regularly replicated to ensure the reproducibility of the measurements. The data are available in supplementary material, Table S2.

To account for changes in seawater δ^{18}O values due to changing sea level and ice volume, a correction factor from Duplessy et al. (2007) was applied, assuming a decrease of -0.008 $\pm$ 0.0002 ‰ per meter of global sea-level rise and using the sea-level reconstruction of Bates et al. (2014). The effect of these corrections on the δ^{18}O values is 0.56 ‰.

4.4. *LA-ICP-MS trace element analysis*

The LA-ICP-MS measurements were performed using a nanosecond 193 nm ArF* excimer-based Analyte G2 laser ablation system (Teledyne Photon Machines) coupled to an Agilent 8800 tandem ICP-MS instrument (Agilent Technologies) via 1 mm ID PEEK tubing of 1 m length and a glass mixing bulb and chamber (Glass Expansion), at the Atomic and Mass Spectrometry – A&MS research unit of Ghent University (Belgium). All analytes were monitored in no-gas mode (with a vented collision/reaction cell). An overview of the nuclides selected for monitoring and the corresponding dwell times is provided in the Table S3 of the Supplementary material.

For quantification purposes, a bracketing approach that consists of performing five consecutive analyses using 1.5 mm line scans of five different glass references materials BCR-2G, BHVO-2G, BIR-1G, GSD-1G, and GSE-1G of the United States Geological Survey (USGS) was employed before and after analyzing according to a line scan over the length of a polished speleothem sample (Fig. 1.A). To compensate for a slight slope of the speleothem samples, the laser beam focus (Z position) was corrected every 2 mm. Samples and standards were ablated using the same instrument settings and data acquisition conditions which were as follows: a circular laser spot size of 50 µm diameter, energy density of 4 J cm^{-2}, repetition rate of 20 Hz, dosage of 20 shots per position and a lateral scan speed of 50 µm s^{-1}. HDIP software (version 1.3.) was used to synchronize the transient ICP-MS data to the time stamps in laser log files. Subtraction of the background signal was performed based on the gas blank signal for all nuclides monitored and the calibration approach was based on external calibration in combination with internal standardization based on the $^{43}Ca^{+}$ signal. The trace element data were averaged by applying a 10 point-running mean (dataset including reference material is available in Table S4 of the supplementary material).

4.5. *µXRF trace elemental mapping*

High-resolution elemental abundance maps of the polished sample surfaces were produced using the M4 Tornado micro-X-ray fluorescence (µXRF) scanner (Bruker nano GmbH) at the VUB, Brussels, Belgium. The µXRF mapping was performed along a 2D grid with 25 µm spacing, a spot size of 25 µm and an integration time of 5 ms per pixel. The X-ray source was operated under maximum energy settings (600 µA, 50 kV) with no source filters. This µXRF mapping approach resulted in qualitative information on the distribution of the elements in the form of elemental maps.

4.6. *Clumped isotopes analysis*

A total of 226 measurements (9 samples, each replicated between 6 and 11 times, together with 123 standard measurements with 1 replicate equivalent to in between 450 and 550 µg of pure carbonate powder) were carried out to obtain clumped isotope values in the AMGC (Archaeology, Environmental Changes and Geo-Chemistry) stable isotope lab at the VUB, Brussels, Belgium using a Nu-Carb carbonate sample preparation system combined with a Nu Instruments Perspective-IS-IRMS, as descripted in De Vleeschouwer et al. (2021). Possible contamination is monitored by scrutinizing raw Δ_{49} values for high deviations from the mean. The ETH standards are measured following the recommendations of Kocken et al. (2019) with a sample-to-standard ratio of 1:1. Analyses and results are monitored in the lab using the Easotope software (John and Bowen, 2016). The carbonate standards ETH-2, IAEA-C1 and IAEA-C2 are systematically measured and compared to InterCarb values (Bernasconi et al., 2021) for quality control purposes. The raw measured Δ_{47} values are processed using the IUPAC isotopic parameters (Brand et al., 2010; Daëron et al., 2016; Petersen et al., 2019) and converted to the ICDES 90 °C scale, using the most recent values for the ETH-1, ETH-3, and ETH-4 carbonate reference materials (Bernasconi et al., 2021) within the ClumpyCrunch software (Daëron, 2021). The average Δ_{47} values for each sample are converted into temperatures using the Anderson et al. (2021) calibration. Both analytical and calibration uncertainties are propagated to calculate the final uncertainties on the temperatures derived. The average temperature uncertainty is calculated to be 1.9°C (1SE). The data are available in Table S5 of the supplementary material.

The drip-water $\delta^{18}O_w$ is calculated using Δ_{47}-derived temperatures and the $\delta^{18}O$ value of the calcite from the same speleothem level using the equation of Daëron et al. (2019). The final uncertainties are calculated by propagating the analytical uncertainties of both Δ_{47}-

derived temperatures and $\delta^{18}O$ values, as well as the equation uncertainties of Daëron et al. (2021).

The ETH 1-4, IAEA-C1 and IAEA-C2 standards have been measured over one entire year at the AMGC-VUB lab. The long-term repeatability of Δ_{47} for all standards (after the data processing described above) is 0.027 ‰ (1SE). The calculated $\delta^{13}C$, $\delta^{18}O$ and Δ_{47} of the clumped-isotope standards are compared to the expected values as follows (Table 1). The Δ_{47} values are compared to the most recent values from Bernasconi et al. (2021). The $\delta^{13}C$ and $\delta^{18}O$ values for ETH 1-4 as well as the $\delta^{18}O$ values for IAEA-C1 and IAEA-C2 are compared to Bernasconi et al. (2018) instead, while the $\delta^{13}C$ of IAEA-C1 and IAEA-C2 are compared to Rozanski et al. (1992). The difference between the values measured in this study and the expected values is considered negligible (lower than the SE associated with the carbonate reference materials) for $\delta^{13}C$, $\delta^{18}O$ and Δ_{47}. These comparisons are used as a means of quality control for the measurements. Also, it is important to note that the IAEA-C1 and IAEA-C2 powders used in this study are from different batches than those used in the InterCarb study (Bernasconi et al., 2021). Based on comparison between two different standard batches, IAEA-C2 powder appears to be homogenous, confirming its value as a standard for clumped isotope analyses. However, the difference between measured and expected values for Δ_{47} IAEA-C1 is larger (0.01 ‰; Table 1) and therefore additional data are required for IAEA-C1 to verify its homogeneity.

Table 1: Isotopic measurement results ($\delta^{13}C$, $\delta^{18}O$ and Δ_{47}) for the ETH1-4 and IAEA-C1 and IAEA-C2 standards calibrated against three ETH reference materials. References (Ref) represent the follow: 1. This study – one year of measurement; 2. Bernasconi et al. (2021); 3. Bernasconi et al. (2018); 4. Rozanski et al. (1992). SD and SE are at the 1 sigma level.

Samples	N	$\delta^{13}C$_VPDB	SD	$\delta^{18}O$_VPDB	SD	Δ_{47}	SE	Ref	Difference		
									$\delta^{13}C$	$\delta^{18}O$	Δ_{47}
ETH-1	132	2.01	0.2	-2.44	0.2	0.2080	0.0069	1	-0.01	0.25	0.0028
	Expected values	2.02	0.03	-2.19	0.04	0.2052	0.0031	2, 3			
ETH-2	119	-10.17	0.2	-18.91	0.2	0.2065	0.0042	1	0	0.22	-0.0021
	Expected values	-10.17	0.06	-18.69	0.11	0.2086	0.003	2, 3			
ETH-3	115	1.72	0.2	-1.77	0.2	0.6084	0.007	1	0.01	-0.01	-0.0048
	Expected values	1.71	0.02	-1.78	0.06	0.6132	0.0027	2, 3			
ETH-4	114	-10.15	0.09	-18.85	0.2	0.4533	0.0042	1	0.05	0.16	0.0028
	Expected values	-10.2	0.03	-18.69	0.11	0.4505	0.0035	2, 3			
IAEA-C1	43	2.44	0.09	-2.89	0.3	0.3125	0.0048	1	0.02	0.57	0.0107
	Expected values	2.42	0.33	-2.32	0.03	0.3018	0.0025	2, 3, 4			
IAEA-C2	50	-8.2	0.2	-9.13	0.4	0.6466	0.0048	1	0.05	0.13	0.0057
	Expected values	-8.25	0.31	-9.00	0.05	0.6409	0.003	2, 3, 4			

4.7. *Dual clumped isotopes analysis*

Dual clumped isotope analysis (i.e, analysis of Δ_{48} alongside Δ_{47} in CO_2 evolved from phosphoric acid digestion of carbonates) has been performed at the Goethe University in Frankfurt using an automated preparation line HAL (Hofmann's Auto Line) that is connected to the dual inlet of a MAT 253plus gas source mass spectrometer (Fiebig et al., 2019). The sampled layer is taken at 27.3 cm, called I-B2-27.3. Data were acquired within a single session lasting from 31/03/2023 to 10/06/2023. In a first step, mass spectrometric m/z 47-49 intensities of each cycle were corrected for a negative background that is continuously monitored on half mass cup 47.5, using cup-specific, iteratively determined scaling factors (Fiebig et al., 2021). Background corrected raw δ^{45}-δ^{47} values were then further processed using D47crunch in its pooled mode (Daëron, 2021) and CO_2 equilibrated at 25°C and 1000°C, respectively, as anchors. Final Δ_{47} and Δ_{48} values are reported on the CDES 90 and compared to the CDES 90 calibration provided by Fiebig et al. (2021). Uncertainties are provided as fully propagated 2SE. Long-term repeatability for this session is 7.0 ppm for Δ_{47} and 25.0 ppm for Δ_{48} (1SD). This compares well with the predicted shot noise limits of 7.0 ppm and 23.4 ppm characteristic of the applied analytical conditions, i.e., m/z 44 ion beam intensity of 16000 mV and a total ion counting time of 2600 s (13 acquisitions with 10 cycles and 20 seconds integration time). All data (replicate values of equilibrated gases, carbonate standards and samples, their corresponding mean values and 2SE, repeatabilities of Δ_{47} and Δ_{48} measurements, a, b and c-factors determined using D47 crunch; Daëron, 2021) can be found in Supplementary material Table S6.

4.8. *Archeological dating model*

The chronology of the Châtelperronian and especially regional durations in western Europe are hampered by the evolution of the ^{14}C calibration curve (IntCal13 into IntCal20, Reimer et al., 2013, 2020). It is important to use the new radiocarbon calibration curve (IntCal20) because it takes into consideration the radiocarbon time dilation, related to the Laschamp geomagnetic excursion, around 41 ka BP (Bard et al., 2020). This may impact the length of overlap between Neanderthal and anatomically modern humans in Eurasia (Bard et al., 2020). Therefore, we used the archaeological synthesis based on the most recent ^{14}C calibration curve IntCal20 (Brad et al., 2020; Djakovic et al., 2022; Fourcade et al., 2022; Rios-Garaizar et al., 2022; Guérin et al., 2023). We also remodel the Châtelperronian time-range from the Ormesson site, using the ages of Bodu et al. (2017), with the same method as Fourcade et al. (2022). The most reliable age is integrated in a Bayesian chronological model (ChronoModel v. 2.0.18, Lanos and Dufresne, 2019). The recalculated age can be found in supplementary material, Table S7.

5. RESULTS

5.1. *Speleothem description*

Three discontinuities (D1, D2 and D3) are identified, allowing the recognition of 3 different growth phases (I-B1, 2 and 3; Fig. 2). At 30.1 cm from the top, a thin detrital layer (D1) marks the transition from layered white opaque and relatively porous, columnar calcite to translucent beige and more compact, elongated columnar calcite (between I-B3 and I-B2; Fig. 2). The µXRF maps indicate higher concentrations of K and Fe at the D1 (Fig. 3; Fig. S3 to 6 for the high-resolution maps). Between 28.8 and 27.4 cm from the top, a gradual change in lithology is observed with a whitening of the calcite. The top of I-B2 records 2 detrital layers (Fig. 2). A first one occurs at 25.4 cm (D2) and shows millimetric-sized dissolution features, leading to an irregular layer. Subsequently, a ~3 mm-thick beige-grey translucent calcite layer is deposited, which, except for the color, is relatively similar to the former calcite, and ends with a more visible detrital layer 25.6 cm from the top (D3; Fig. 2). Bright-orange calcite layers (red layer) are deposited with the incorporation of several millimetric-sized clay clumps in the first six to seven layers, followed by a progressive transition to finely layered white calcite, returning to characteristics more similar to the base of the speleothem I-B (I-B3; Fig. 2). The µXRF maps indicate higher concentrations of Al, K, Fe and Si at the D2, D3 levels and the red layer (Fig. 3; Fig. S4 to 6 for the high-resolution maps), suggesting deposition of thin clay layers, incorporated in the calcite.

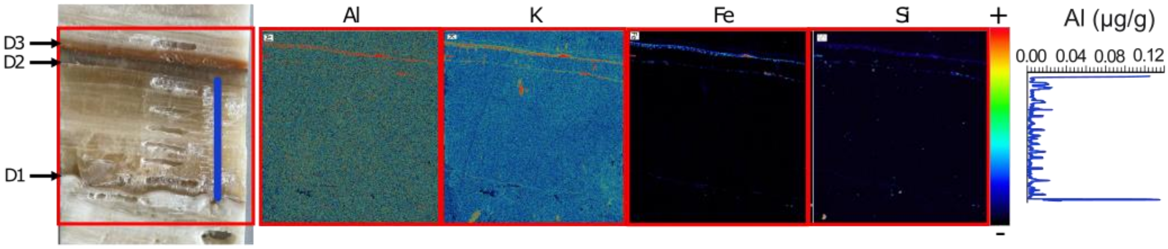

Figure 3: **Trace elemental µXRF maps to highlight the I-B2 discontinuities.** Photography of the I-B2 speleothem with the location of the µXRF-scan (red squares) with the spatial distribution of Al, Ti, K, Fe and Si, and the Al content (blue line). Discontinuities 1 to 3 are indicated using the letter D.

5.2. *Age model*

A total of 11 U/Th dates were obtained for this study, all focusing on part I-B of the speleothem (Table S1). The ages are given in ka before 1950 CE. The part I-B1 stops growing at 76.6 ka BP (+/- 0.3 ka; sample 11 in figure 2). The speleothems started to grow again after D1, at 57.7 ka BP (+/- 0.6 ka; sample 10 in figures 2 & 4). This part corresponds to part I-B2, which includes 9 dates. The second discontinuity (D2) is dated between 42 ka BP (+/- 1.5 ka; sample 3 in figures 2 & 4) and 37 ka BP (+/- 0.1 ka; sample 2 in figures 2 & 4), which is followed by the red layer and the last discontinuity (D3). Part I-B3 is dated to the Holocene with an associated age of 11.5 ka BP (+/- 0.01 ka; sample 1 in figure 2).

For the age model, we used the uncertainties due to the sampling (± 0.2 cm), calculated assuming a constant deposition rate between 2 ages. The age model indicates a low deposition rate of 2.6 µm/year on average (Fig. 4).

Between D1 and D2, no other discontinuities were identified in the µXRF maps (Fig. 3). The Al content also records variations that are relatively small compared to the Al content recorded at the discontinuities (maximum 0.03 µg/g between D1 and D2 compared to 0.5 µg/g at D2 and 0.8 µg/g at D1; Fig. 3), a strong argument for the absence of other discontinuities, even undetectable by macroscopic observation. Even if an eventual hiatus cannot be completely eliminated, the absence of even a small detrital layer makes this option less probable. The production of additional ages, especially between samples 5 and 6 would ameliorate the precision of the age model, however, the low growth rate limits the thickness of deposited calcite (only a few millimeters) hampering additional sampling~~.~~ Moreover, related to the slow but most probably variable growth rate in Interstadial and Stadial climate conditions, we acknowledge some limitations due to the linear fit obtained with StalAge (not always necessarily linear, but this is the case of our study). Additional discussion on the age model (linear fit including all the ages or linear fit only between 2 ages), and potential implications on our interpretation is included in the supplementary material.

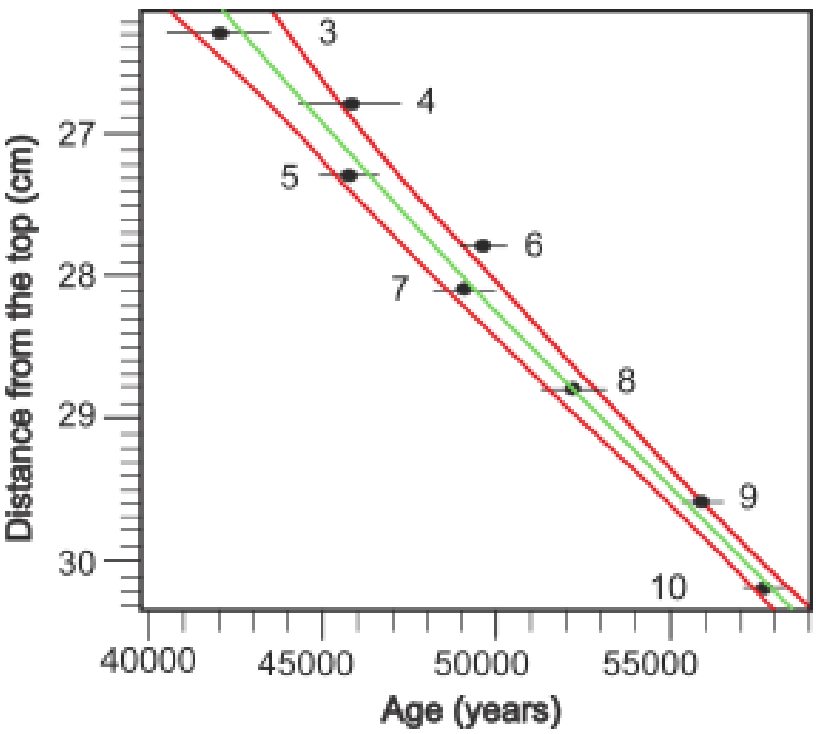

Figure 4: Age model between D1 and D2. The dating used for this age model correspond to the red dating in Fig. 2. The age model is calculated at 2SE.

5.3. *Isotopic equilibrium*

Firstly, the I-B2 part mainly consists of white and opaque columnar calcite with very fine laminations (typical of flowstone) with some larger euhedral spar crystals (typical of local small pools). The calcite appears to have been deposited continuously (in continuation of underlying layers). Based on the age-depth model, I-B2 starts to grow at 57.7 ka BP and continues until 37.0 ka BP. The chronology indicates a low deposition rate of 2.6 μm/a, which is rather low compared to other central European speleothem deposition rates such as in Bunker cave, Germany (between 10 and 70 μm/a, Weber et al., 2018) or in Villars cave in southwest of France (between 100 μm/a during the D/O 12 and 10 μm/a during the cold periods; Genty et al., 2003, 2005 and 2010). Low deposition rate of speleothems favors precipitation close to isotopic equilibrium, by reducing the CO_2-degassing and/or the evaporation of drip water (Daëron et al., 2019; Guo & Zhou, 2019). Also, the deposition of columnar crystals and the presence of micro pool structures suggest slow calcite precipitation under a water film or in subaqueous conditions, which limits rapid CO_2-degassing. Following Daëron et al. (2019), these are fundamental conditions to record the original clumped isotope signal.

Secondly, as suggested by Hendy (1971), the isotopic disequilibrium may be verified using stable isotope ratio values by investigating the $\delta^{13}C$ and $\delta^{18}O$ correlations and the isotopic variations along single growth layers. The high covariance between $\delta^{13}C$ and $\delta^{18}O$ suggests potential disequilibrium. Here, the covariance is low for the whole data set (Pearson coefficient R^2 of 0.14) (Fig. 5.A). Similarly, the correlation coefficients of the main climatic events (individual DO events), highlighted by the different colors in Figure 5.A, are low (R2 between 0.06 and 0.41; Fig. 5.A). The orange period (from 56.3 to 50.0 ka) shows higher correlation (R^2 of 0.41), but it is still quite low. Furthermore, the isotopic variations along a single layer are tested by measuring $\delta^{13}C$ - $\delta^{18}O$ five times on five different single growth layers

(Fig. 2 and Fig. 5.B). The results indicate a variation lower than 0.2‰ for $\delta^{13}C$ and for $\delta^{18}O$. The limited variations of $\delta^{18}O$ within a single line, combined with the absence of $\delta^{13}C$ - $\delta^{18}O$ correlation do not indicate potential disequilibrium.

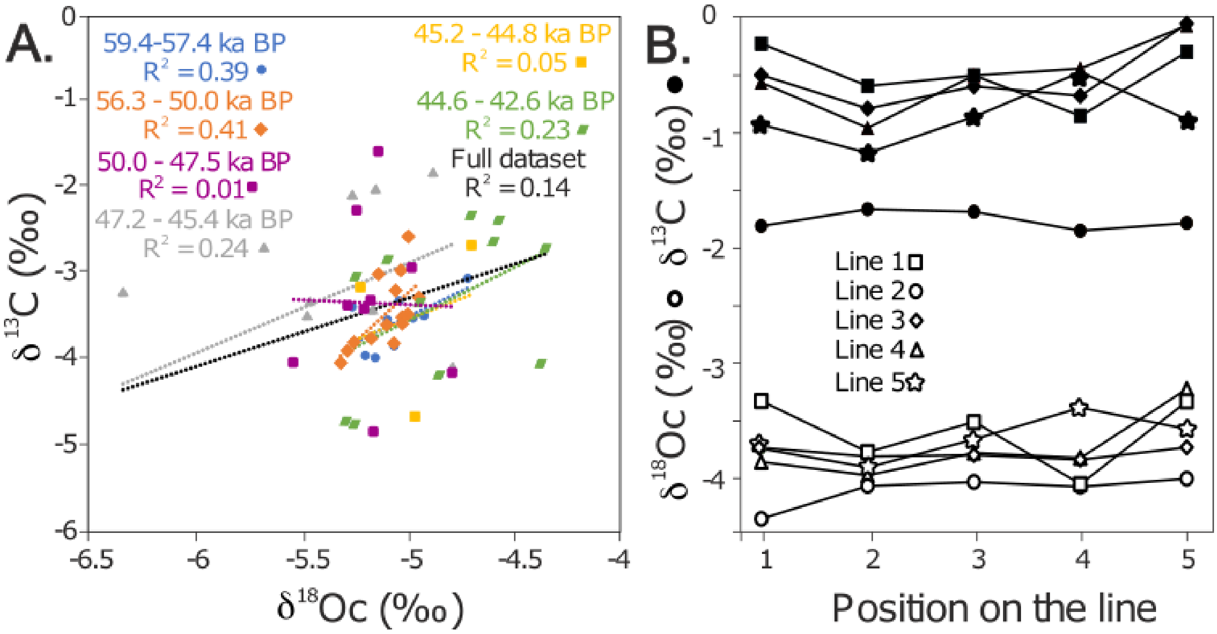

Figure 5: isotopic measurements for the Hendy test. A. calcite $\delta^{18}O_c$ vs $\delta^{13}C$ comparison with coefficient correlation associated with Greenland Interstadial (GI) -16 (blue circle), section 2 (orange diamond), GI-12 (grey triangle), Greenland Stadial (GS) -11 (yellow scare), GI-11 (green parallelogram) and the full database (black) and B. $\delta^{18}O_c$ (empty symbols) and $\delta^{13}C$ (filled symbols) values at 5 positions on 5 different single growth layers (labelled 1 to 5, associated with different symbols), as shown in Fig. 1.

Thirdly, dual clumped isotope thermometry (high precision analysis of Δ_{48} together with Δ_{47}) allows to determine to which extent the isotopic composition of a given carbonate sample has been affected by kinetics (Bajnai et al., 2020; Fiebig et al., 2021). Dual clumped isotope analysis reveals the absence of any significant kinetic bias in sample I-B2-27.3 (taken in the I-B2 part at 27.3 cm from the top – at 45.77 ka), as measured Δ_{47} (0.6513‰ $\pm$ 0.0027‰; 1SE) and Δ_{48} (0.2667‰ $\pm$ 0.0096‰; 1SE) values plot both within 2SE and 1SE indistinguishable from equilibrium (Fig. 6). Moreover, the temperature of 6.4 ± 1.7 °C obtained based on dual clumped isotope thermometry overlaps with the temperature of 6.4 ± 1.5 °C inferred from Δ_{47} thermometry. The sampled layer at 27.3 cm from the top exhibits the highest growth rate (Between dating samples 4 and 5). If no significant kinetic effect is observed for the highest growth rate, no kinetic effect would be noticeable if the growth rates were lower. Based on these observations, the I-B2 speleothem represents an excellent candidate for temperature reconstructions based on the application of the Δ_{47} thermometer.

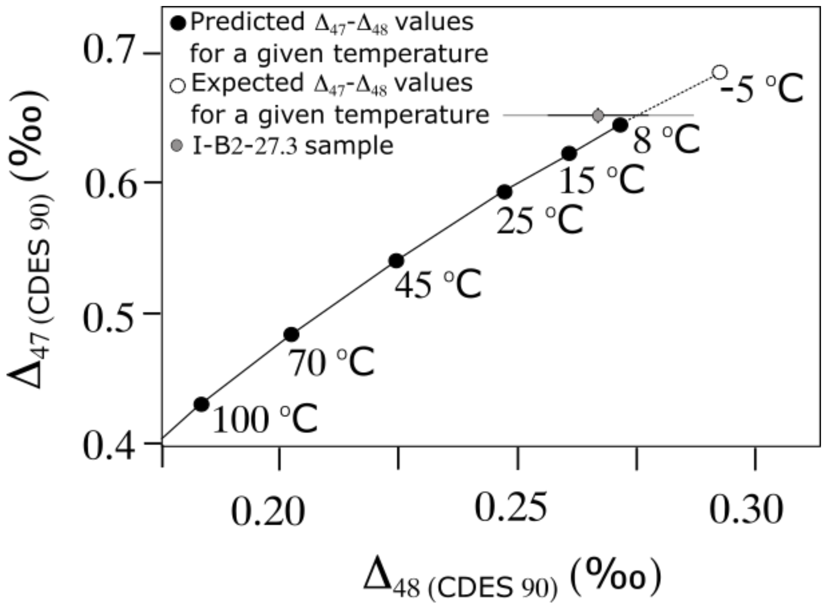

Figure 6: isotopic equilibrium highlighted by Δ_{47}-Δ_{48} measurement. Dual clumped isotope composition of sample I-B2-27.3, relative to predicted and expected equilibrium Δ_{47} - Δ_{48} values (Fiebig et al., 2021). Δ_{48} uncertainties are at 1 SE (black) and 2 SE (grey). Δ_{47} uncertainties are at 2 SE (black).

5.4. *Elemental & isotopic climatic records*

Calcite $\delta^{18}O$ and $\delta^{13}C$ values vary between -3.8 to -5.8 ‰ and -1.5 to -5 ‰, respectively (Fig. 7). The $\delta^{13}C$ curve appears congruent to the $\delta^{18}O$ data, except from 56.7 to 50.2 ka BP where the $\delta^{13}C$ value exhibits more variability than the $\delta^{18}O$ value. From the older to the younger part, the $\delta^{18}O$ variations start with a decrease of 0.5 ‰, followed by a plateau at around -4.5 ‰ until 50.2 ka BP. The $\delta^{18}O$ values exhibit small negative peaks, but overall remain relatively stable compared to $\delta^{13}C$. Between 50.2 and 43.8 ka, the $\delta^{18}O$ and $\delta^{13}C$ curves show stronger, with higher values of -3.7 ‰ and -1.5 ‰ respectively around 45.7 ka and 48.3 ka and lower values of -5.7‰ and -5‰ respectively around 47.7 and 46.9 ka (Fig. 7).

The concentrations of the elements Zn and P show a progressive increase through the section with larger variations (Fig. 7). The Mg, Sr, and Ba concentrations display stronger variability (Fig. 7). The Mg concentration (between 0.1 μg/g up to 0.3 μg/g) displays the same relative variations as Sr (ranging from 14 to 48 μg/g) and Ba (ranging from 1 to 9 μg/g) with R^2 values of up to 0.47 from 59.2 to 56.4 ka and 0.47 from 47.9 to 49.2 ka BP. However, from 45.0 to 42.4 ka BP, the Sr concentrations display variations similar to those for $\delta^{13}C$, while the Mg concentrations decrease progressively, resulting on a poor agreement between the two elements (R^2 = 0.01). Furthermore, [P] and [Zn] show good agreement with $\delta^{13}C$ variations from 47.9 to 42.4 ka (R^2 = 0.48 and 0.56 respectively).

The samples display T- Δ_{47} values between 2.8 ± 2.1 °C and 14.8 ± 2.6 °C (Fig. 7). Four samples, from the most recent part of the record, overlap within error with the modern cave air temperature (ca. 10.2 °C), while the remaining five constrain colder temperatures (Fig. 7). Higher T- Δ_{47} correspond to the lower carbonate $\delta^{18}O$ values (Fig. 7). Reconstructions of the drip water $\delta^{18}O$ ($\delta^{18}O_w$) value provide a range from -7.2 ± 0.6 ‰ to -5.3 ± 0.4 ‰, lower than or in the range of the modern cave $\delta^{18}O_w$ (-7.5 ‰) (Fig. 7). While at low resolution, the $\delta^{18}O_w$ curve follows the variations of the $\delta^{13}C$ curve (Fig. 7).

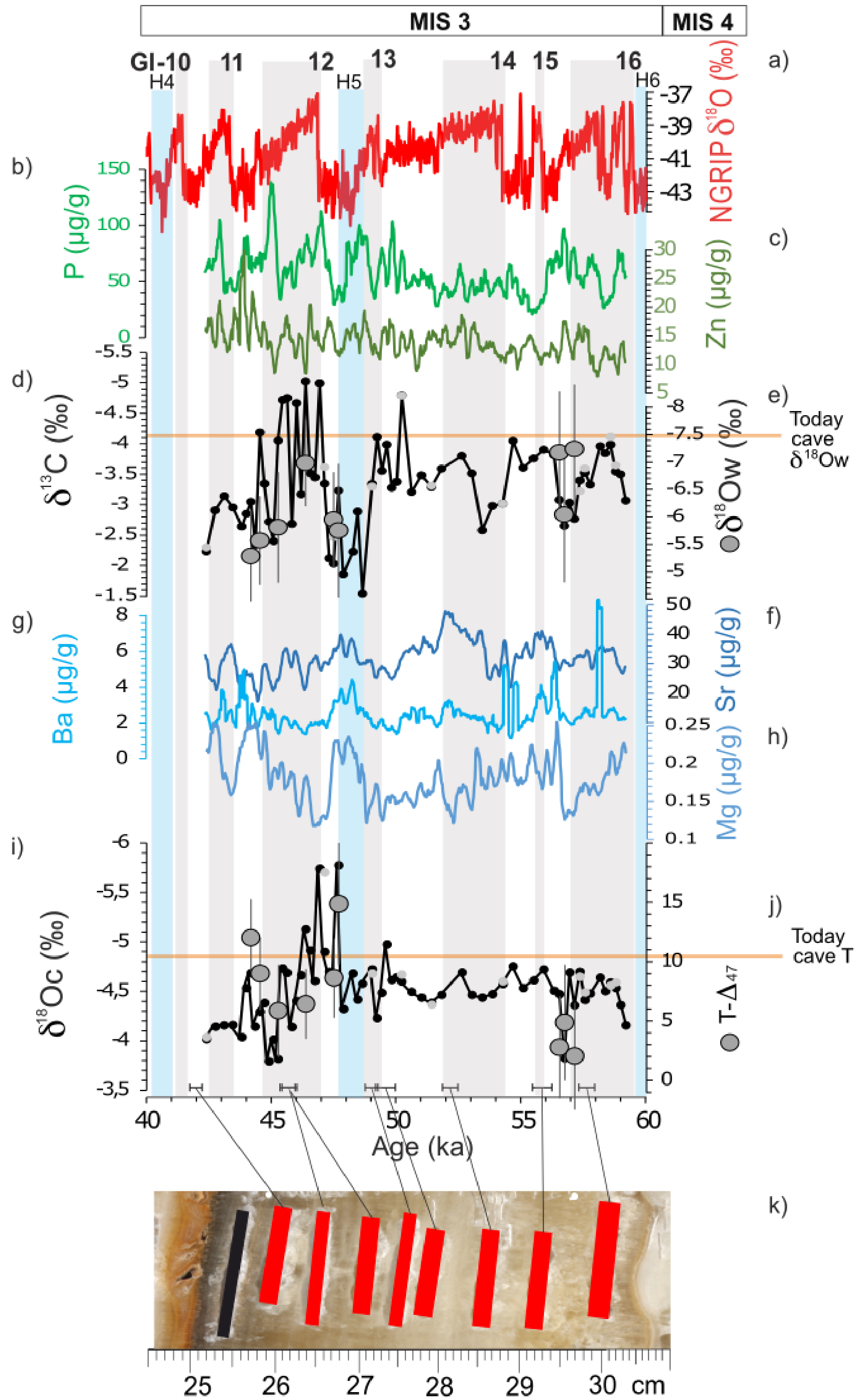

Figure 7: Isotopic and elemental data from I-B2 speleothem. Data from I-B2 speleothem from the top to the bottom: the NGRIP $\delta^{18}O$ value of the ice (Svensson et al., 2018) (a), the contents of Zn, P (b, c), the $\delta^{13}C$ curve, with the drip water $\delta^{18}O$ datapoints reconstructed from the

combination of clumped isotopes and the calcite $\delta^{18}O$ value (d and e), the contents of Sr, Ba and Mg (f, g and h), the calcite $\delta^{18}O$ curve with the T-Δ_{47} reconstructed from clumped isotope measurements (i and j). The grey dots correspond to the replicates of the bulk isotopic measurements. The ages and their 2SE uncertainties are plotted at the bottom of the graph and are correlated to the I-B2 speleothem photograph (k). The GIs within the MIS 3 are highlighted using grey rectangles. The H-events are marked using blue rectangles.

6. CLIMATIC PROXIES INTERPRETATION

The $\delta^{13}C$ values reflect soil thickening and/or soils activity (Fairchild et al., 2001; Huang et al., 2001; Treble et al., 2003; Borsato et al., 2007). Low values are associated with denser vegetation above the cave (Genty et al., 2003; Tremaine et al., 2011). A decrease in $\delta^{13}C$ suggests favorable conditions for soil development. Negative $\delta^{13}C$ peaks are often correlated with high P and Zn concentrations. Low concentrations of P and Zn indicate a reduction of soil activity at the surface – respectively vegetation dieback (Fairchild et al., 2001; Borsato et al., 2007; Allan et al., 2018) and soil flushing events (Hartland et al., 2012). An increase in [P] and [Zn] therefore suggests more soil activity. Negative peaks of $\delta^{13}C$ can be correlated to high [P] and [Zn], indicating more active soil.

The vegetation is also linked to water availability. Different proxies provide information on hydrology. The $\delta^{18}Oc$ records both temperature and the $\delta^{18}Ow$, associated with rainfall amount, regional circulation system and/or through cave-specific processes, transferring the climatic signatures (McDermott, 2004, 2011; Tremaine et al., 2011; Lachniet, 2009). This proxy is promising when combined with [Mg], [Ba] and [Sr]. These elements are interpreted to reflect water availability (Fairchild et al., 2001; Huang et al., 2001; McDermott, 2004), especially in the case of the Han-sure-Lesse cave system (Verheyden et al., 2008; Allan et al., 2018) and the Bunker cave (Weber et al., 2018). An agreement between increase in [Ba], [Mg] and [Sr] and decrease in the isotopic compositions ($\delta^{13}C$ and $\delta^{18}Oc$) suggests warmer and/or wetter conditions. However, [Mg], [Ba] and [Sr] in antiphase may indicate incongruent dissolution, occurring during drier conditions (Vansteenberge et al., 2020).

Despite this information, these proxies provide only qualitative information. To obtain quantitative climatic information, we have determined Δ_{47}-derived temperatures (T(Δ_{47})) and used these temperatures to reconstruct the $\delta^{18}O_w$. Today, the $\delta^{18}O$ drip water at the site study correlate with the $\delta^{18}O$ rainwater with a 5 to 6 months residence time of the water in the epikarst (Van Rampelbergh et al., 2014). The $\delta^{18}O_w$ changes would indicate changes in circulation schemes and/or moisture source. Combined with [Ba], [Mg], [Sr] and bulk isotopic measurement, this approach traces changes in water availability.

7. DISCUSSION

7.1. *A climatic amelioration at the MIS 3 onset*

This study focuses only on the second part, labelled I-B, from 17.6 to 37.4 cm from top, and particularly on the I-B2 facies, covering the early MIS 3. The D1 discontinuity indicates a hiatus of ~18 ka, covering the end of MIS 4 and the beginning of early MIS 3 (Table S1), which can be related to the Heinrich H6 cold event (Sánchez-Goñi et al., 2013). Its presence suggests poor conditions for speleothem deposition, in agreement with models indicating rapidly (in ~5 ka) decreasing mean annual air temperatures to 0 °C or below starting from 80 ka to ~55 ka in Belgium (Govaerts et al., 2016). However, the climatic conditions may have warmed before, as the I-B2 part started growing around 59.2 ka (dating sample 10 = 57.7 ka ± 0.2 ka), associated with GI-16 (Greenland Interstadial 16 = GI-16, after H6) in the NGRIP $\delta^{18}O$ values (Svensson et al., 2008). Until 57.9 ka, the $\delta^{13}C$ and $\delta^{18}Oc$ values show a decrease of 1 ‰ and 0.5 ‰, respectively (Fig. 7). Low $\delta^{13}C$ values are associated with denser vegetation above the cave (Genty et al., 2003). The decreasing trends in $\delta^{13}C$ suggest favorable conditions for soil development during the GI-16.

At 56.7 ka, the GS-15 is marked by a progressive increase in $\delta^{13}C$ and abrupt shift to higher $\delta^{18}Oc$. The T(Δ_{47}) remain stable during the GS-15, suggesting limited temperature variations. The obtained temperatures are colder than today (between 2 and 4.8 °C; Fig. 7) but warmer than during the H6 associated with the D1 (cessation of growth) and as also supported by the model (Govaerts et al., 2016). The reconstructed $\delta^{18}O_w$ values show changes by up to 1 ‰ (Fig. 7) during the GS-15, indicating that $\delta^{18}Oc$ is dominated by $\delta^{18}Ow$ rather than temperature variations. Since the Sr, Ba and Mg concentrations remain low (Fig. 7), reflecting high water availability (Fairchild et al., 2001; Huang et al., 2001; McDermott, 2004; Verheyden et al., 2008; Allan et al., 2018), the $\delta^{18}Ow$ changes are more likely related to changes in circulation schemes and/or moisture source with enriched $\delta^{18}Ow$ corresponding to northern Atlantic Ocean precipitation origin (McDermott et al., 2011).

The data show a climatic amelioration from the H6, as supported by models with the disappearance of permafrost in Belgium, associated with a temperature increase, triggering permafrost melting (Govaerts et al., 2016). This melted water could account for sufficient water within the cave system to precipitate speleothem in near isotopic equilibrium. The GS-15 was warmer than H6, as also indicated by models showing that permafrost completely disappeared in Belgium during GS-15.

7.2. *A weak climatic signal in speleothems during the DO14*

By comparing with the NGRIP $\delta^{18}O$ changes, the DO-14 event is not well recognized in the I-B2 speleothem. The DO-14 shows only variations in $\delta^{13}C$ values and [Sr]. No significant variations are observed in $\delta^{18}O$ or other elemental measurements. Furthermore, this part is associated with more covariance between $\delta^{13}C$ and $\delta^{18}Oc$ values ($R^2 = 0.41$; Fig. 5.A), which may suggest the influence of kinetic effects during this period only. Interestingly, the DO-14 is also not well-delineated or only partially marked in the isotopic signal of speleothems from southwestern France (Genty et al., 2003, 2005, 2010; Wainer et al., 2009; Fig.) or from Bunker cave in Germany (Weber et al., 2018). The absence of a strong DO-14 signal in European speleothems may suggest a delay between the warm and humid conditions during DO-14 and the onset of speleothem growth. Additional investigations are necessary to formulate hypotheses explaining the weak expression of the DO-14 in speleothem records.

7.3. *Climatic responses to the DO 13 and 12 events in Belgium*

The GI-13 is associated with wet conditions (small negative peak in $\delta^{13}C$ values and low [Mg], [Ba] and [Sr]; Fig. 7). The water availability may have increased the development of vegetation above the cave, as indicated by lower $\delta^{13}C$ values and a positive concentration peak in P and Zn (Fairchild et al., 2001; Borsato et al., 2007; Allan et al., 2018; Hartland et al., 2012). However, a fast and major increase in $\delta^{13}C$ (2.3 ‰) during the following stadial (GS-13) suggests a rapid decrease in surface soil activity due to colder and drier climate conditions (increase in δ^{18}Oc, [Mg], [Ba] and [Sr]). During the DO-12, similar variations are observed in the δ^{18}Oc, [Ba], [Mg] and [Sr] and in the δ^{13}C, [P] and [Zn] (Fig. 7; $R^2 > 0.4$), suggesting warmer and/or wetter conditions during the interstadials and colder and/or drier climate during the stadials. The absolute T-Δ_{47} confirms the warm condition with cave temperatures relatively similar or slightly higher (within the uncertainties) especially at the onset of the GI-12 (14.9 ± 2.6 °C). Due to uncertainties linked to our age model (see discussion in supplementary material), the second high temperature data point (12.0 ± 1.6 °C) may correspond to the onset of the DO-11. However, it is interesting to note that the temperature decreases significantly (equivalent to stadial temperatures) withing the DO-12. This temperature decrease is concomitant to high water availability (low [Mg], [Ba], [Sr]) and stronger development of soil above the cave (lower δ^{13}C values and positive peak of [P]). The δ^{13}C decreases 0.8 kyr before the δ^{18}Oc. This time lag may reflect a delay between a climatic amelioration (more negative δ^{18}Oc and high T(Δ_{47})) and change in vegetation (more negative δ^{13}C and increase of [P]; Fig. 7). This likely derives from a delay between the enhancement in temperature and moisture availability as the δ^{13}C and the $\delta^{18}O_w$ decrease simultaneously (Fig. 7). Alternatively, the time lag can also result from poor soil preservation during GS-12, associated with the H5-event, which does not permit a fast return of the vegetation, as suggested by Genty et al. (2003), or a combination of both.

7.4. *Climatic responses to the DO events in western Europe*

By comparing the I-B2 records with those embedded in other continental and marine archives important similarities appear to reflect the large-scale response to the DO millennial scale oscillations in Europe: speleothems from the south (France; Genty et al., 2003) or closer to the ice sheets (Ireland; Fankhauser et al., 2016), recorded DO events similar to the I-B2 speleothem. Also, the good agreement between the NGRIP δ^{18}O and stable isotopic speleothem records, such as I-B2, Villars cave (south-west part of France; Genty et al., 2003, 2005; Wainer et al., 2009) (Fig. 8) or even in Soreq cave (Israel; Bar-Matthews et al., 2000) confirm this larger spatial distribution and evidence of rapid responses to DO. The I-B2 speleothem data also confirm the previous qualitative observations, with warm and wet climate associated with GIs and cold and dry conditions to GSs, as suggested by the deposition rate and the elemental and isotopic measurements of European MIS 3 speleothems (Genty et al., 2003, 2005, 2010; Wainer et al., 2009; Pons-Branchu et al., 2010; Weber et al., 2018), and by the dust records from Maar Lakes (Sirocko et al., 2016).

The comparisons between different MIS 3 recorded in Europe also provide information on the permafrost front. The I-B2 speleothem-initiated growth after the H6 event agrees with the onset of milder conditions at the beginning of the MIS 3, as also found in the Maar lakes (Eifel in Germany; Sirocko et al., 2016) and marine archives (Shackleton et al., 2000; Sánchez-Goñi et al., 2008; through the presence of the cold-planktonic foraminiferal species and ice-rafted debris; Fig. 8). However, a delay of ~2 kyr compared to southern European speleothems is noticeable. The Villars speleothem (Genty et al., 2003) records a shorter phase of extremely cold climate between to 67.4 ($\pm$ 0.9 ka) and 61.2 ka ($\pm$ 0.6 ka) compared to I-B2 phase (76.6 ($\pm$ 0.3) to 59.2 ka), indicating that the cold period started earlier and ended later in the northern regions. The location of I-B2 speleothem could account for this delay, as it is closer to the ice sheets and/or the permafrost (Govaerts et al., 2016).

These comparisons also highlight differences in vegetation and moisture availability in Europe. The δ^{13}C values of the I-B2 speleothem are generally higher than those from other southern European speleothems and the Bunker cave in Germany (Weber et al., 2018; latitudinal Northward to I-B2), indicating more restricted vegetational activity and soil development in Belgium. Likewise, [Mg] remains low relative to those of the German Bu2 speleothem that shows values ranging between 25 and 1500 µg/g (Weber et al., 2018). The Bunker cave [Mg] suggest an increase of water availability and precipitation enhancement from 52 to 51 ka BP, followed, from 47 to 43 ka BP, by less precipitation (Fig. 8; Weber et al., 2018), as also supported by the pollen data from Eifel Lake, with a transition from thermophilous trees to boreal forests (Sirocko et al., 2016). The Mg concentration in the I-B2 interval advocates for relatively more moisture in Belgium, compared to Germany during the entire MIS 3. This wetter condition likely reflects the more marine climate in Belgium. However, the aluminum (Al) content shows an increase throughout the MIS 3 in Belgium (Fig. 8), which may suggest an enhancement of detrital input into the speleothem (Fairchild and Treble, 2009) triggered by the accumulation of fine particles in drier environments. The I-B2 data likely confirm a drier north European climate through the MIS 3.

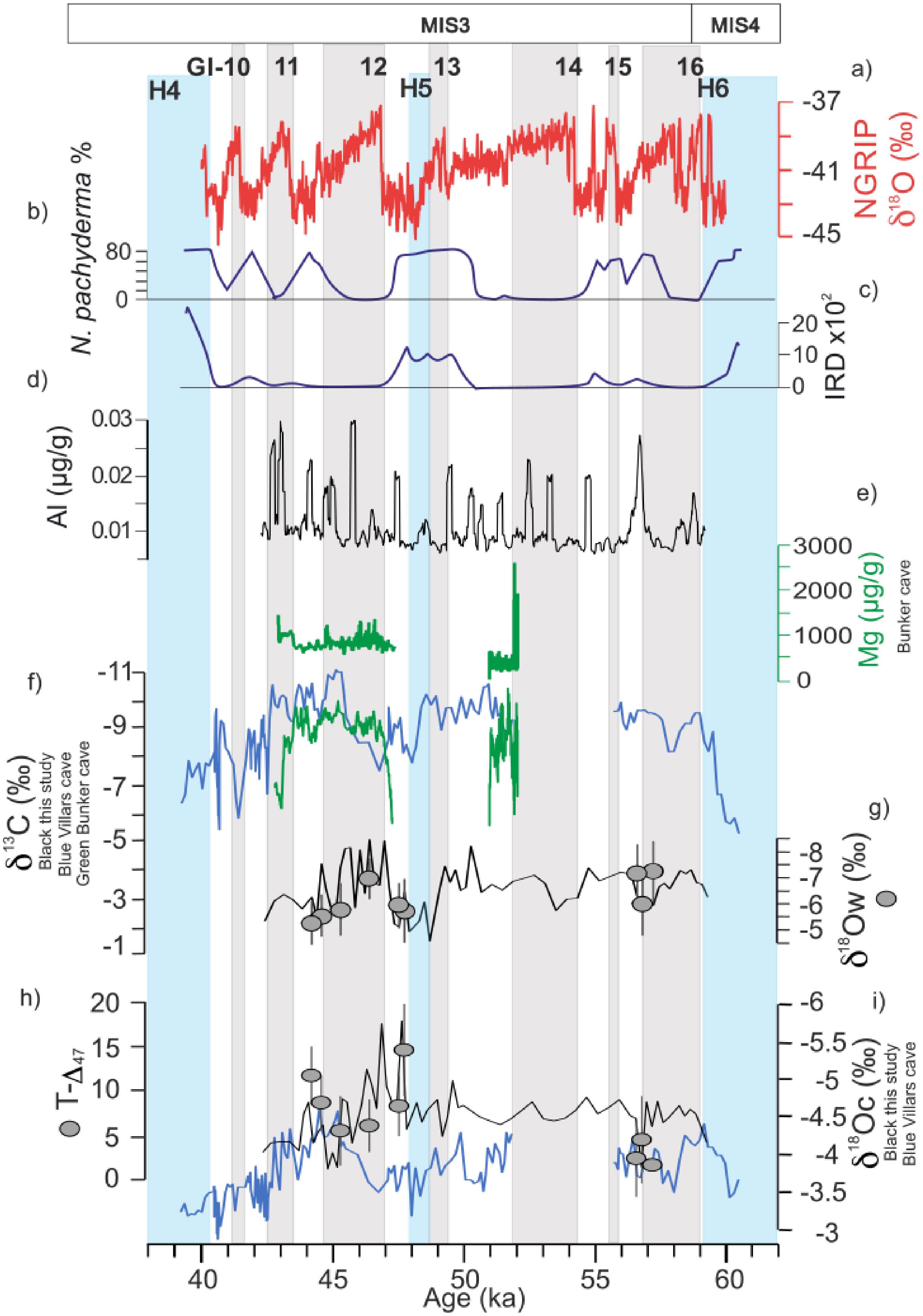

Figure 8: Comparison of I-B2 data with those from other continental and marine records. From the top to the bottom, with the NGRIP $\delta^{18}O$ values for ice (Svensson et al., 2008) (a), *N. pachyderma* s. percentage (b) and IRD content from MD04-2845 (Sánchez-Goñi et al., 2008)

(c), the Al content from this study (d), Mg content (green from Bunker cave; Weber et al. (2018)) (e), the calcite $\delta^{13}C$ curve (black this article, blue from Villars cave; Genty et al. 2003, green from Bunker cave; Weber et al. 2018) (f) with the reconstructed $\delta^{18}Ow$ from this study (g), and the T-Δ_{47} (h) plotted with the calcite $\delta^{18}O$ curve (black this article, blue from Villars cave; Genty et al. 2003) (i). The GIs correspond to the grey rectangles and the H-events are marked using blue rectangles.

7.5. *A gradual paleoclimatic degradation in western Europe*

The geochemical and petrographic description of the I-B2 speleothem suggests a rapid degradation (cooling and drying) of the climate conditions during the most recent part of the record. The two observed detrital hiatuses (D2 and D3), the incorporation of millimetric clay clumps, and the high concentrations of Al, K, Fe and Si at the D2 and D3 levels in the μXRF maps (Fig. 3) also arguments in support of cooling and drying. The D2 deposited between 42.4 ka (± 0.1 ka) and 37.1 ka (± 0.1 ka), while the D3 occurs between I-B2 (37.1 ka ± 0.1 ka) and I-B1 (above the red layer) at the onset of the Holocene at 11.5 ka (± 0.1 ka). These observations all point towards a growth cessation, resulting from a climatic degradation and soil reduction. From 43.4 ka, the increase in $\delta^{13}C$, $\delta^{18}Oc$ values and [Mg] suggest less vegetation activity due to colder and drier condition (Fig. 8). The [Mg] and the [Sr] are in antiphase, which may indicate incongruent dissolution, occurring during drier conditions (Vansteenberge et al., 2020).

A similar climate deterioration is observed in other European MIS 3 speleothems, however, with a different timing. North to South in western Europe, the climatic degradation occurred gradually (Fig. 8):

i) in Germany, from 44.4 ka (marked by increased $\delta^{13}C$ and [Mg]) to 42.8 ka (marked by the growth stop during MIS 3; Weber et al., 2018),

ii) in Belgium, from 43.4 ka (increased $\delta^{13}C$ and $\delta^{18}Oc$, [Mg] and [Sr]) to 37.1 ± 0.1 ka (short restart of speleothem growth), followed by a growth cessation (D3), and,

iii) in the southwest of France, from 41.7 ka (less marked DO oscillations in the isotopic measurements) to 31.8 ka (speleothem growth cessation; Genty et al., 2003, 2010).

An increasing time lag of climate degradation (considering the age uncertainties) is observed from the north to the south in western Europe. The increase in $\delta^{13}C$ speleothem shows that the progressive southward cooling is associated with slowing down of vegetation activity. At around ~42-40 ka, growth of European speleothems stopped (Genty et al. (2003; 2010) and this study), suggesting colder conditions and potential presence of permafrost until the start of the Holocene.

7.6. *Implication of a southward climatic degradation to the Neanderthal extinction*

This period of climatic degradation is also marked by the Neanderthal-modern human interchange. To investigate a possible connection between climate change and the end of Neanderthals, we use the most recent updated archaeological synthesis that remodeled key sites in western Europe with the new ^{14}C calibration curve, based on the Châtelperronian culture (Fig. 9; Brad et al., 2020; Djakovic et al., 2022; Fourcade et al., 2022; Rios-Garaizar et al., 2022; Guérin et al., 2023; see methodology). The recalculated Châtelperronian interval (using the new ^{14}C calibration curve) from Ormesson site is larger than the other sites in western Europe (Fig. 9). This difference may be explained by large uncertainties on the original ages and methodological (model) issues, as in general, the intervals of Fourcade et al. (2022) are longer than those in the other datasets (Fig. 9). This may be due to the probability distributions, which are higher because the Chrono Model integrated all of the ages and their uncertainties. The updated archaeological synthesis also includes Neanderthal remains (Devièse et al., 2021; Abrams, 2023; Guérin et al., 2023; Fig. 9). Dated last Neanderthal remains, in the northwest Europe, are estimated between 44.2 and 40.6 ka (Devièse et al., 2021) and between 40.8 and 40.4 ka (Djakovic et al., 2022), similar to remains found in France (Djakovic et al., 2022).

In Figure 9, climatic deterioration periods (marked by elemental and/or isotopic measurements and stop of growth) are compared to the archeological synthesis showing the occupation of Neanderthal. Any climatic role in the last occupation of Neanderthals in western Europe would imply a southward extinction of Neanderthals, following climatic degradation. However, no southward extinction of Neanderthal has previously been observed in north-western Europe (e.g., Hublin & Roebroeks,2009; Roebroeks et al., 2011). A link between climate and disappearance of the Neanderthals could be unlikely, regardless of the model used for this archaeological synthesis. (Fig. 9). This comparison suggests that climate and/or vegetation changes did not play an important role in the extinction of the Neanderthals in western Europe, as suggested by the model of Timmermann (2020). Our data therefore provides better environmental constraints on human mobility versus climate changes models.

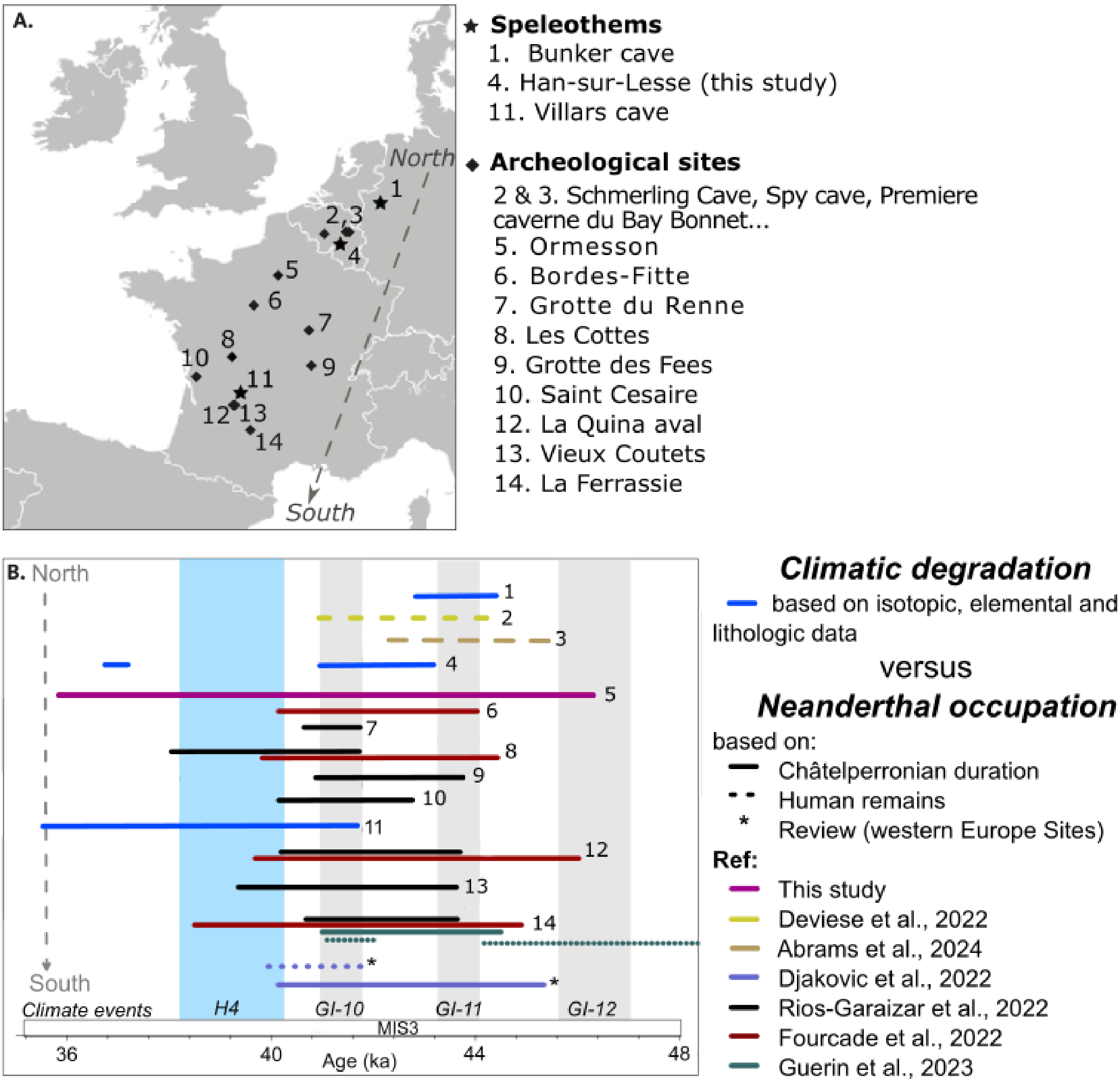

Figure 9: **Climatic degradation compared to the Neanderthal occupations in Europe.** A. Map of western Europe with the locations of the paleoclimatic (stars) and archeological (diamonds) records used in this study, against latitude (from north at the top to south at the bottom). B. Ages of the climatic degradation (associated with elemental and/or isotopic measurements) in speleothem archives compared with the Neanderthals occupations, based on the most recent studies from north- to south-western Europe. The numbers correspond to the speleothems and archeological sites presented in panel A. The references correspond to the articles that published the age interval of the Neanderthal occupations. The climatic events are highlighted by grey rectangles for the GI and a blue rectangle for the H-4 event.

CONCLUSIONS

This unique continental MIS 3 record sheds new light on the climatic variability of this period in western Europe and the potential consequences on Neanderthals human replacement by *Homo sapiens*. Using state-of-the-art methods, we show that the speleothem precipitated close to isotopic equilibrium, which enables the confident use of clumped-isotope thermometry and allows to dissociate MIS 3 temperature from hydrology signals. Our results confirm a warm and humid climate during the interstadials and cold and dry conditions during the stadials, with an estimated difference in temperature of approximately 7°C. The start of MIS 3 is marked by a climatic amelioration, following the cold H5 at the end of MIS 4, allowing the permafrost to melt and the speleothem to grow. Interestingly, DO-14 is not well-recorded in our speleothem, similar to expressions in other western European speleothems (excluding the Iberian margin). The DO-12 is characterized by a 1-ka delay between $\delta^{13}C$ and $\delta^{18}O$, with $\delta^{18}O$ changing before $\delta^{13}C$, in agreement with observations in southwest France. This interval is interpreted to reflect a delay between climatic improvement and the availability of water leading to the development of vegetation. Finally, we document a climatic deterioration extending from north to south. However, based on the most recent archaeological synthesis, no comparable southward decline of Neanderthal occupation is observed. Therefore, a link between climate change and extinction of the Neanderthals in western Europe is not supported.

REFERENCES

Abrams, G. C. M. G. (2023). *Close encounters of the third kind?: Neanderthals and modern humans in Belgium, a bone story* (Doctoral dissertation, Leiden University).

Abrams, G., Devièse, T., Pirson, S., De Groote, I., Flas, D., Jungels, C., ... & Di Modica, K. (2024). Investigating the co-occurrence of Neanderthals and modern humans in Belgium through direct radiocarbon dating of bone implements. *Journal of Human Evolution*, *186*, 103471.

Affek, H. P., Bar-Matthews, M., Ayalon, A., Matthews, A., & Eiler, J. M. (2008). Glacial/interglacial temperature variations in Soreq cave speleothems as recorded by 'clumped isotope'thermometry. *Geochimica et Cosmochimica Acta*, *72*(22), 5351-5360.

Affek, H.P., Zaarur, S., 2014. Kinetic isotope effect in CO2 degassing: Insight from clumped and oxygen isotopes in laboratory precipitation experiments. Geochim. Cosmochim. Acta 143, 319–330. https://doi.org/10.1016/j.gca.2014.08.005

Allan, M., Deliège, A., Verheyden, S., Nicolay, S., Quinif, Y., Fagel, N., 2018. Evidence for solar influence in a Holocene speleothem record (Père Noël cave, SE Belgium). Quat. Sci. Rev. 192, 249–262.

Anderson, N.T., Kelson, J.R., Kele, S., Daëron, M., Bonifacie, M., Horita, J., Mackey, T.J., John, C.M., Kluge, T., Petschnig, P., 2021. A unified clumped isotope thermometer calibration (0.5–1,100 C) using carbonate-based standardization. Geophys. Res. Lett. 48, e2020GL092069.

Bajnai, D., Guo, W., Spötl, C., Coplen, T. B., Methner, K., Löffler, N., ... & Fiebig, J. 2020. Dual clumped isotope thermometry resolves kinetic biases in carbonate formation temperatures. *Nature Communications*, *11*(1), 4005.

Balzeau, A., Turq, A., Talamo, S., Daujeard, C., Guérin, G., Welker, F., ... & Gómez-Olivencia, A. 2020. Pluridisciplinary evidence for burial for the La Ferrassie 8 Neandertal child. *Scientific reports*, *10*(1), 21230.

Banks, W.E., d'Errico, F., Peterson, A.T., Kageyama, M., Sima, A., Sánchez-Goñi, M.-F., 2008. Neanderthal extinction by competitive exclusion. PLoS One 3, e3972.

Bar-Matthews, M., Ayalon, A., Kaufman, A., 2000. Timing and hydrological conditions of Sapropel events in the Eastern Mediterranean, as evident from speleothems, Soreq cave, Israel. Chem. Geol. 169, 145–156.

Bard, E., Heaton, T. J., Talamo, S., Kromer, B., Reimer, R. W., & Reimer, P. J. 2020. Extended dilation of the radiocarbon time scale between 40,000 and 48,000 y BP and the overlap between Neanderthals and Homo sapiens. *Proceedings of the National Academy of Sciences*, *117*(35), 21005-21007.

Bates, S.L., Siddall, M., Waelbroeck, C., 2014. Hydrographic variations in deep ocean temperature over the mid-Pleistocene transition. Quat. Sci. Rev. 88, 147–158. https://doi.org/10.1016/j.quascirev.2014.01.020

Bernasconi, S. M., Müller, I. A., Bergmann, K. D., Breitenbach, S. F., Fernandez, A., Hodell, D. A., ... & Ziegler, M. 2018. Reducing uncertainties in carbonate clumped isotope analysis through consistent carbonate-based standardization. *Geochemistry, Geophysics, Geosystems*, *19*(9), 2895-2914.

Bernasconi, S.M., Daëron, M., Bergmann, K.D., Bonifacie, M., Meckler, A.N., Affek, H.P., Anderson, N., Bajnai, D., Barkan, E., Beverly, E., Blamart, D., Burgener, L., Calmels, D., Chaduteau, C., Clog, M., Davidheiser-Kroll, B., Davies, A., Dux, F., Eiler, J., Elliott, B., Fetrow, A.C., Fiebig, J., Goldberg, S., Hermoso, M., Huntington, K.W., Hyland, E., Ingalls, M., Jaggi, M., John, C.M., Jost, A.B., Katz, S., Kelson, J., Kluge, T., Kocken, I.J., Laskar, A., Leutert, T.J., Liang, D., Lucarelli, J., Mackey, T.J., Mangenot, X., Meinicke, N., Modestou, S.E., Müller, I.A., Murray, S., Neary, A., Packard, N., Passey, B.H., Pelletier, E., Petersen, S., Piasecki, A., Schauer, A., Snell, K.E., Swart, P.K., Tripati, A., Upadhyay, D., Vennemann, T., Winkelstern, I., Yarian, D., Yoshida, N., Zhang, N., Ziegler, M., 2021. InterCarb: A Community Effort to Improve Interlaboratory Standardization of the Carbonate Clumped Isotope Thermometer Using Carbonate Standards. Geochemistry, Geophys. Geosystems 22, 1–25. https://doi.org/10.1029/2020GC009588

Bodu, P., Salomon, H., Lacarrière, J., Baillet, M., Ballinger, M., Naton, H. G., & Théry-Parisot, I. 2017. Un gisement châtelperronien de plein air dans le Bassin parisien: les Bossats à Ormesson (Seine-et-Marne). *Gallia Préhistoire*, (57), 3-64.

Böhm, E., Lippold, J., Gutjahr, M., Frank, M., Blaser, P., Antz, B., ... & Deininger, M. 2015. Strong and deep Atlantic meridional overturning circulation during the last glacial cycle. *Nature*, *517*(7532), 73-76.

Bond, G., Broecker, W., Johnsen, S., McManus, J., Labeyrie, L., Jouzel, J., Bonani, G., 1993. Correlations between climate records from North Atlantic sediments and Greenland ice. Nature 365, 143–147.

Bonniver, I. (2011). *Etude hydrogéologique et dimensionnement par modelisation du" système-traçage" du réseau karstique de Han-sur-Lesse (Massif de Boine-Belgique)* (Doctoral dissertation, UNamur-Université de Namur).

Borsato, A., Frisia, S., Fairchild, I.J., Somogyi, A., Susini, J., 2007. Trace element distribution in annual stalagmite laminae mapped by micrometer-resolution X-ray fluorescence: implications for incorporation of environmentally significant species. Geochim. Cosmochim. Acta 71, 1494–1512.

Brand, W.A., Assonov, S.S., Coplen, T.B., 2010. Correction for the 17O interference in δ(13C) measurements when analyzing CO2 with stable isotope mass spectrometry (IUPAC Technical Report). Pure Appl. Chem. 82, 1719–1733. https://doi.org/10.1351/PAC-REP-09-01-05

Burlet, C., Vanbrabant, Y., Piessens, K., Welkenhuysen, K., & Verheyden, S. (2015). Niphargus: A silicon band-gap sensor temperature logger for high-precision environmental monitoring. *Computers & geosciences*, *74*, 50-59.

Cacho, I., Grimalt, J. O., Pelejero, C., Canals, M., Sierro, F. J., Flores, J. A., & Shackleton, N. 1999. Dansgaard-Oeschger and Heinrich event imprints in Alboran Sea paleotemperatures. *Paleoceanography*, *14*(6), 698-705.

Cheng, H., Edwards, R.L., Shen, C.-C., Polyak, V.J., Asmerom, Y., Woodhead, J., Hellstrom, J., Wang, Y., Kong, X., Spötl, C., 2013. Improvements in 230Th dating, 230Th and 234U half-life values, and U–Th isotopic measurements by multi-collector inductively coupled plasma mass spectrometry. Earth Planet. Sci. Lett. 371, 82–91.

Columbu, A., Chiarini, V., Spötl, C., Benazzi, S., Hellstrom, J., Cheng, H., & De Waele, J. 2020. Speleothem record attests to stable environmental conditions during Neanderthal–modern human turnover in southern Italy. *Nature ecology & evolution*, *4*(9), 1188-1195.

Daëron, M., 2021. Full propagation of analytical uncertainties in Δ47 measurements. Geochemistry, Geophys. Geosystems 22, e2020GC009592.

Daëron, M., Blamart, D., Peral, M., Affek, H.P., 2016. Absolute isotopic abundance ratios and the accuracy of Δ<inf>47</inf> measurements. Chem. Geol. https://doi.org/10.1016/j.chemgeo.2016.08.014

Daëron, M., Drysdale, R.N., Peral, M., Huyghe, D., Blamart, D., Coplen, T.B., Lartaud, F., Zanchetta, G., 2019. Most Earth-surface calcites precipitate out of isotopic equilibrium. Nat. Commun. https://doi.org/10.1038/s41467-019-08336-5

Daëron, M., Guo, W., Eiler, J., Genty, D., Blamart, D., Boch, R., Drysdale, R., Maire, R., Wainer, K., Zanchetta, G., 2011. 13C18O clumping in speleothems: Observations from natural caves and precipitation experiments. Geochim. Cosmochim. Acta 75, 3303–3317. https://doi.org/10.1016/j.gca.2010.10.032

Dansgaard, W., Johnsen, S. J., Clausen, H. B., Dahl-Jensen, D., Gundestrup, N. S., Hammer, C. U., ... & Bond, G. 1993. Evidence for general instability of past climate from a 250-kyr ice-core record. *nature*, *364*(6434), 218-220.

Dayet, L., d'Errico, F., & Garcia-Moreno, R. 2014. Searching for consistencies in Châtelperronian pigment use. *Journal of Archaeological Science*, *44*, 180-193.

De Vleeschouwer, D., Peral, M., Marchegiano, M., Füllberg, A., Meinicke, N., Pälike, H., Auer, G., Petrick, B., Snoeck, C., Goderis, S., Claeys, P., 2021. Plio-Pleistocene Perth Basin water temperatures and Leeuwin Current dynamics (Indian Ocean) derived from oxygen and clumped isotope paleothermometry. Clim. Past Discuss. 2021, 1–40. https://doi.org/10.5194/cp-2021-151

Degioanni, A., Bonenfant, C., Cabut, S., Condemi, S., 2019. Living on the edge: Was demographic weakness the cause of Neanderthal demise? PLoS One 14, e0216742.

Demidenko, Y. E. & Škrdla, P. Lincombian-Ranisian-Jerzmanowician Industry and South Moravian Sites: a Homo sapiens Late Initial Upper Paleolithic with Bohunician Industrial Generic Roots in Europe. J Paleo Arch 6, 17 (2023).

Devièse, T., Abrams, G., Hajdinjak, M., Pirson, S., De Groote, I., Di Modica, K., Toussaint, M., Fischer, V., Comeskey, D., Spindler, L., 2021. Reevaluating the timing of Neanderthal disappearance in Northwest Europe. Proc. Natl. Acad. Sci. 118, e2022466118.

Djakovic, I., Key, A., Soressi, M., 2022. Optimal linear estimation models predict 1400–2900 years of overlap between Homo sapiens and Neandertals prior to their disappearance from France and northern Spain. Sci. Rep. 12, 15000.

Duplessy, J.C., Roche, D.M., Kageyama, M., 2007. The deep ocean during the last interglacial period. Science (80-.). 316, 89–91.

Edwards, R.L., Chen, J.H., Wasserburg, G.J., 1987. 238U234U230Th232Th systematics and the precise measurement of time over the past 500,000 years. Earth Planet. Sci. Lett. 81, 175–192.

d'Errico, F., Sanchez-Goñi, M.F., 2003. Neandertal extinction and the millennial scale climatic variability of OIS 3. Quat. Sci. Rev. 22, 769–788.

Fairchild, I.J., Baker, A., Borsato, A., Frisia, S., Hinton, R.W., McDERMOTT, F., Tooth, A.F., 2001. Annual to sub-annual resolution of multiple trace-element trends in speleothems. J. Geol. Soc. London. 158, 831–841.

Fairchild, I.J., Treble, P.C., 2009. Trace elements in speleothems as recorders of environmental change. Quat. Sci. Rev. 28, 449–468.

Fankhauser, A., McDermott, F., Fleitmann, D., 2016. Episodic speleothem deposition tracks the terrestrial impact of millennial-scale last glacial climate variability in SW Ireland. Quat. Sci. Rev. 152, 104–117. https://doi.org/10.1016/j.quascirev.2016.09.019

Fiebig, J., Bajnai, D., Löffler, N., Methner, K., Krsnik, E., Mulch, A., & Hofmann, S. 2019. Combined high-precisionΔ 48 andΔ 47 analysis of carbonates. *Chemical Geology*, *522*, 186-191.

Fiebig, J., Daëron, M., Bernecker, M., Guo, W., Schneider, G., Boch, R., Bernasconi, S.M., Jautzy, J., Dietzel, M., 2021. Calibration of the dual clumped isotope thermometer for carbonates. Geochim. Cosmochim. Acta 312, 235–256.

Flas, D. 2011. The Middle to Upper Paleolithic transition in Northern Europe: the Lincombian-Ranisian-Jerzmanowician and the issue of acculturation of the last Neanderthals. *World Archaeology*, *43*(4), 605-627.

Fourcade, T., Goñi, M.F.S., Lahaye, C., Rossignol, L., Philippe, A., 2022. Environmental changes in SW France during the Middle to Upper Paleolithic transition from the pollen analysis of an eastern North Atlantic deep-sea core. Quat. Res. 110, 147–164.

Genty, D., & Deflandre, G. (1998). Drip flow variations under a stalactite of the Pere Noel cave (Belgium). Evidence of seasonal variations and air pressure constraints. *Journal of Hydrology*, *211*(1-4), 208-232.

Genty, D., Blamart, D., Ouahdi, R., Gilmour, M., Baker, A., Jouzel, J., Van-Exter, S., 2003. Precise dating of Dansgaard-Oeschger climate oscillations in western Europe from stalagmite data. Nature 421, 833–837. https://doi.org/10.1038/nature01391

Genty, D., Combourieu-Nebout, N., Peyron, O., Blamart, D., Wainer, K., Mansuri, F., Ghaleb, B., Isabello, L., Dormoy, I., von Grafenstein, U., Bonelli, S., Landais, A., Brauer, A., 2010. Isotopic characterization of rapid climatic events during OIS3 and OIS4 in Villars Cave stalagmites (SW-France) and correlation with Atlantic and Mediterranean pollen records. Quat. Sci. Rev. 29, 2799–2820. https://doi.org/10.1016/j.quascirev.2010.06.035

Genty, D., Nebout, N.C., Hatté, C., Blamart, D., Ghaleb, B., Isabello, L., 2005. Rapid climatic changes of the last 90 kyr recorded on the European continent. Comptes Rendus Geosci. 337, 970–982.

Gicqueau, A., Schuh, A., Henrion, J., Viola, B., Partiot, C., Guillon, M., ... & Maureille, B. 2023. Anatomically modern human in the Châtelperronian hominin collection from the Grotte du Renne (Arcy-sur-Cure, Northeast France). *Scientific Reports*, *13*(1), 12682.

Govaerts, J., Beerten, K., ten Veen, J., 2016. Weichselian permafrost depth in the Netherlands: a comprehensive uncertainty and sensitivity analysis. Cryosph. 10, 2907–2922.

Gravina, B., Bachellerie, F., Caux, S., Discamps, E., Faivre, J. P., Galland, A., ... & Bordes, J. G. 2018. No reliable evidence for a Neanderthal-Châtelperronian association at La Roche-à-Pierrot, Saint-Césaire. *Scientific Reports*, *8*(1), 15134.

Guérin, G., Aldeias, V., Baumgarten, F., Goldberg, P., Gómez-Olivencia, A., Lahaye, C., Madelaine, S., Maureille, B., Philippe, A., Sandgathe, D., 2023. A Third Neanderthal Individual from La Ferrassie Dated to the End of the Middle Palaeolithic. PaleoAnthropology 2023, 98–118.

Hartland, A., Fairchild, I.J., Lead, J.R., Borsato, A., Baker, A., Frisia, S., Baalousha, M., 2012. From soil to cave: Transport of trace metals by natural organic matter in karst dripwaters. Chem. Geol. 304, 68–82.

Higham, T., Douka, K., Wood, R., Ramsey, C.B., Brock, F., Basell, L., Camps, M., Arrizabalaga, A., Baena, J., Barroso-Ruíz, C., 2014. The timing and spatiotemporal patterning of Neanderthal disappearance. Nature 512, 306–309.

Heinrich, H. 1988. Origin and consequences of cyclic ice rafting in the northeast Atlantic Ocean during the past 130,000 years. *Quaternary research*, *29*(2), 142-152.

Hemming, S. R. 2004. Heinrich events: Massive late Pleistocene detritus layers of the North Atlantic and their global climate imprint. *Reviews of Geophysics*, *42*(1).

Higham, T., Jacobi, R., Julien, M., David, F., Basell, L., Wood, R., ... & Ramsey, C. B. 2010. Chronology of the Grotte du Renne (France) and implications for the context of ornaments and human remains within the Châtelperronian. *Proceedings of the National Academy of Sciences*, *107*(47), 20234-20239.

Holzkämper, S., Spötl, C., Mangini, A., 2005. High-precision constraints on timing of Alpine warm periods during the middle to late Pleistocene using speleothem growth periods. Earth Planet. Sci. Lett. 236, 751–764.

Huang, Y., Fairchild, I.J., Borsato, A., Frisia, S., Cassidy, N.J., McDermott, F., Hawkesworth, C.J., 2001. Seasonal variations in Sr, Mg and P in modern speleothems (Grotta di Ernesto, Italy). Chem. Geol. 175, 429–448.

Huber, C., Leuenberger, M., Spahni, R., Flückiger, J., Schwander, J., Stocker, T. F., ... & Jouzel, J. 2006. Isotope calibrated Greenland temperature record over Marine Isotope Stage 3 and its relation to CH4. *Earth and Planetary Science Letters*, *243*(3-4), 504-519.

Hublin, J. J., Spoor, F., Braun, M., Zonneveld, F., & Condemi, S. 1996. A late Neanderthal associated with Upper Palaeolithic artefacts. *Nature*, *381*(6579), 224-226.

Hublin, J. J., & Roebroeks, W. (2009). Ebb and flow or regional extinctions? On the character of Neandertal occupation of northern environments. *Comptes Rendus Palevol*, *8*(5), 503-509.

Hublin, J. J., Talamo, S., Julien, M., David, F., Connet, N., Bodu, P., ... & Richards, M. P. 2012. Radiocarbon dates from the Grotte du Renne and Saint-Césaire support a Neandertal origin for the Châtelperronian. *Proceedings of the National Academy of Sciences*, *109*(46), 18743-18748.

John, C.M., Bowen, D., 2016. Community software for challenging isotope analysis: First applications of 'Easotope' to clumped isotopes. Rapid Commun. Mass Spectrom. 30, 2285–2300. https://doi.org/10.1002/rcm.7720

Johnsen, S. J., Clausen, H. B., Dansgaard, W., Fuhrer, K., Gundestrup, N., Hammer, C. U., ... & Steffensen, J. P. 1992. Irregular glacial interstadials recorded in a new Greenland ice core. *Nature*, *359*(6393), 311-313.

Kindler, P., Guillevic, M., Baumgartner, M., Schwander, J., Landais, A., & Leuenberger, M. 2014. Temperature reconstruction from 10 to 120 kyr b2k from the NGRIP ice core. *Climate of the Past*, *10*(2), 887-902.

Kluge, T., Affek, H.P., Marx, T., Aeschbach-Hertig, W., Riechelmann, D.F.C., Scholz, D., Riechelmann, S., Immenhauser, A., Richter, D.K., Fohlmeister, J., 2013. Reconstruction of drip-water $\delta^{18}O$ based on calcite oxygen and clumped isotopes of speleothems from Bunker Cave (Germany). Clim. Past 9, 377–391.

Kocken, I.J., Müller, I.A., Ziegler, M., 2019. Optimizing the Use of Carbonate Standards to Minimize Uncertainties in Clumped Isotope Data. Geochemistry, Geophys. Geosystems 20, 5565–5577. https://doi.org/10.1029/2019GC008545

Lachniet, M. S. 2009. Climatic and environmental controls on speleothem oxygen-isotope values. *Quaternary Science Reviews*, *28*(5-6), 412-432.

Lanos, P., & Dufresne, P. 2019. ChronoModel version 2.0.Lachniet, 2009

Lisiecki, L. E., & Raymo, M. E., 2005. A Pliocene-Pleistocene stack of 57 globally distributed benthic $\delta^{18}O$ records. *Paleoceanography*, *20*(1).

Locht, J.-L., 2019. La fin du Paléolithique moyen dans le nord de la France. Quaternaire. Revue de l'Association française pour l'étude du Quaternaire 335–350. https://doi.org/10.4000/quaternaire.12456

Locht, J.-L., Hérisson, D., Goval, E., Cliquet, D., Huet, B., Coutard, S., Antoine, P., Feray, P., 2016. Timescales, space and culture during the Middle Palaeolithic in northwestern France. Quaternary International 411, 129–148. https://doi.org/10.1016/j.quaint.2015.07.053

Luetscher, M., Boch, R., Sodemann, H., Spötl, C., Cheng, H., Edwards, R.L., Frisia, S., Hof, F., Müller, W., 2015. North Atlantic storm track changes during the Last Glacial Maximum recorded by Alpine speleothems. Nat. Commun. 6, 6344. https://doi.org/10.1038/ncomms7344

Marín-Arroyo, A.B., Rios-Garaizar, J., Straus, L.G., Jones, J.R., de la Rasilla, M., González Morales, M.R., Richards, M., Altuna, J., Mariezkurrena, K., Ocio, D., 2018. Chronological reassessment of the Middle to Upper Paleolithic transition and early Upper Paleolithic cultures in Cantabrian Spain. PLoS One 13, e0194708.

Matthews, A., Affek, H. P., Ayalon, A., Vonhof, H. B., & Bar-Matthews, M. (2021). Eastern Mediterranean climate change deduced from the Soreq Cave fluid inclusion stable isotopes and carbonate clumped isotopes record of the last 160 ka. *Quaternary Science Reviews*, *272*, 107223.

McDermott, F., 2004. Palaeo-climate reconstruction from stable isotope variations in speleothems: a review. Quat. Sci. Rev. 23, 901–918.

McDermott, F., Atkinson, T.C., Fairchild, I.J., Baldini, L.M., Mattey, D.P., 2011. A first evaluation of the spatial gradients in $\delta^{18}O$ recorded by European Holocene speleothems. Glob. Planet. Change 79, 275–287. https://doi.org/10.1016/j.gloplacha.2011.01.005

Moseley, G.E., Spötl, C., Brandstätter, S., Erhardt, T., Luetscher, M., Edwards, R.L., 2020. NALPS19: Sub-orbital-scale climate variability recorded in northern Alpine speleothems during the last glacial period. Clim. Past 16, 29–50.

Moseley, G.E., Spötl, C., Svensson, A., Cheng, H., Brandstätter, S., Edwards, R.L., 2014. Multi-speleothem record reveals tightly coupled climate between central europe and greenland during marine isotope stage 3. Geology 42, 1043–1046. https://doi.org/10.1130/G36063.1

Nehme, C., Todisco, D., Breitenbach, S.F.M., Couchoud, I., Marchegiano, M., Peral, M., Vonhof, H., Hellstrom, J., Tjallingii, R., Claeys, P., 2023. Holocene hydroclimate variability along the Southern Patagonian margin (Chile) reconstructed from Cueva Chica speleothems. Glob. Planet. Change 222, 104050.

Peel, M. C., Finlayson, B. L., & McMahon, T. A. (2007). Updated world map of the Köppen-Geiger climate classification. *Hydrology and earth system sciences*, *11*(5), 1633-1644.

Petersen, S. V, Defliese, W.F., Saenger, C., Daëron, M., Huntington, K.W., John, C.M., Kelson, J.R., Bernasconi, S.M., Colman, A.S., Kluge, T., Olack, G.A., Schauer, A.J., Bajnai, D., Bonifacie, M., Breitenbach, S.F.M., Fiebig, J., Fernandez, A.B., Henkes, G.A., Hodell, D., Katz, A., Kele, S., Lohmann, K.C., Passey, B.H., Peral, M.Y., Petrizzo, D.A., Rosenheim, B.E., Tripati, A., Venturelli, R., Young, E.D., Winkelstern, I.Z., 2019. Effects of Improved ^{17}O Correction on Interlaboratory Agreement in Clumped Isotope Calibrations, Estimates of Mineral-Specific Offsets, and Temperature Dependence of Acid Digestion Fractionation. Geochemistry, Geophys. Geosystems. https://doi.org/10.1029/2018GC008127

Picin, A., Moroni, A., & Benazzi, S. 2022. The arrival of Homo sapiens in the Near East and Europe. In *Updating Neanderthals* (pp. 321-347). Academic Press.

Pirson, S., Flas, D., Abrams, G., Bonjean, D., Court-Picon, M., Di Modica, K., ... & Semal, P. 2012. Chronostratigraphic context of the Middle to Upper Palaeolithic transition: Recent data from Belgium. *Quaternary International*, *259*, 78-94.

Pons-Branchu, E., Hamelin, B., Losson, B., Jaillet, S., Brulhet, J., 2010. Speleothem evidence of warm episodes in northeast France during Marine Oxygen Isotope Stage 3 and implications for permafrost distribution in northern Europe. Quat. Res. 74, 246–251. https://doi.org/10.1016/j.yqres.2010.06.007

Poulain, A., Rochez, G., Bonniver, I., & Hallet, V. (2015). Stalactite drip-water monitoring and tracer tests approach to assess hydrogeologic behavior of karst vadose zone: case study of Han-sur-Lesse (Belgium). *Environmental Earth Sciences*, *74*, 7685-7697.

Quinif, Y., & Bastin, B. (1994). U/Th dating and pollen analysis of a stalagmitic sequence of the isotopic stage 5 (''Galerie des Vervietois, Grotte de Han''Belgium). Datation uranium/thorium et analyse pollinique d'une sequence stalagmitique du stade isotopique 5 (Galerie des Vervietois, Grotte de Han-sur-Lesse, Belgique). *Comptes Rendus de l'Academie des Sciences. Serie 2;(France)*, *318*(2).

Quinif, Y. (2006). Complex stratigraphic sequences in Belgian caves: Correlation with climatic changes during the middle, the upper Pleistocene, and the Holocene. *Geologica Belgica*. QUINIF, Y. (2017). Le complexe sédimentaire de la Galerie des Verviétois (Grotte de Han-sur-Lesse, Belgique). *Geologica Belgica*.

QUINIF, Y. 2017. Le complexe sédimentaire de la Galerie des Verviétois (Grotte de Han-sur-Lesse, Belgique). *Geologica Belgica*.

Rasmussen, T. L., & Thomsen, E. 2004. The role of the North Atlantic Drift in the millennial timescale glacial climate fluctuations. *Palaeogeography, Palaeoclimatology, Palaeoecology*, *210*(1), 101-116.

Rasmussen, S. O., Bigler, M., Blockley, S. P., Blunier, T., Buchardt, S. L., Clausen, H. B., ... & Winstrup, M. 2014. A stratigraphic framework for abrupt climatic changes during the Last Glacial period based on three synchronized Greenland ice-core records: refining and extending the INTIMATE event stratigraphy. *Quaternary science reviews*, *106*, 14-28.

Reimer, P. J., Bard, E., Bayliss, A., Beck, J. W., Blackwell, P. G., Ramsey, C. B., ... & Van Der Plicht, J. 2013. IntCal13 and Marine13 radiocarbon age calibration curves 0–50,000 years cal BP. *radiocarbon*, *55*(4), 1869-1887.

Reimer, P. J., Austin, W. E., Bard, E., Bayliss, A., Blackwell, P. G., Ramsey, C. B., ... & Talamo, S. 2020. The IntCal20 Northern Hemisphere radiocarbon age calibration curve (0–55 cal kBP). *Radiocarbon*, *62*(4), 725-757.

Roebroeks, W., Hublin, J. J., & MacDonald, K. (2011). Continuities and discontinuities in Neandertal presence: a closer look at northwestern Europe. In *Developments in Quaternary Sciences* (Vol. 14, pp. 113-123). Elsevier.

Romagnoli, F., Chabai, V., Gravina, B., Hérisson, D., Hovers, E., Moncel, M. H., ... & Sykes, R. W. 2022. Neanderthal technological variability: A wide-ranging geographical perspective on the final Middle Palaeolithic. In *Updating Neanderthals* (pp. 163-205). Academic Press.

ROZANSKI, K., STICHLER, W., GONFIANTINI, R., SCOTT, E. M., BEUKENS, R. P., KROMER, B., VAN DER PLICHT, J., 1992. The IAEA ^{14}C Intercomparison exercise 1990. Radiocarbon, **34** 3, 506-519.

Rios-Garaizar, J., Iriarte, E., Arnold, L.J., Sánchez-Romero, L., Marín-Arroyo, A.B., San Emeterio, A., Gómez-Olivencia, A., Pérez-Garrido, C., Demuro, M., Campaña, I., 2022. The intrusive nature of the Châtelperronian in the Iberian Peninsula. PLoS One 17, e0265219.

Ruebens, K., McPherron, S. J., & Hublin, J. J. 2015. On the local Mousterian origin of the Châtelperronian: Integrating typo-technological, chronostratigraphic and contextual data. *Journal of Human Evolution*, *86*, 55-91.

Sánchez Goñi, M. F., Cacho, I., Turon, J. L., Guiot, J., Sierro, F. J., Peypouquet, J. P., ... & Shackleton, N. J. 2002. Synchroneity between marine and terrestrial responses to millennial scale climatic variability during the last glacial period in the Mediterranean region. *Climate dynamics*, *19*, 95-105.

Sanchez-Goñi, M.F.S., Landais, A., Fletcher, W.J., Naughton, F., Desprat, S., Duprat, J., 2008. Contrasting impacts of Dansgaard–Oeschger events over a western European latitudinal transect modulated by orbital parameters. Quat. Sci. Rev. 27, 1136–1151.

Sánchez Goñi, M.F., Bard, E., Landais, A., Rossignol, L., d'Errico, F., 2013. Air–sea temperature decoupling in western Europe during the last interglacial–glacial transition. Nat. Geosci. 6, 837–841.

Scholz, D., & Hoffmann, D. L. (2011). StalAge–An algorithm designed for construction of speleothem age models. *Quaternary Geochronology*, *6*(3-4), 369-382.

Semal, P., Rougier, H., Crevecoeur, I., Jungels, C., Flas, D., Hauzeur, A., ... & van der Plicht, J. 2009. New data on the late Neandertals: Direct dating of the Belgian Spy fossils. *American Journal of Physical Anthropology: The Official Publication of the American Association of Physical Anthropologists*, *138*(4), 421-428.

Severinghaus, J. P., Sowers, T., Brook, E. J., Alley, R. B., & Bender, M. L. 1998. Timing of abrupt climate change at the end of the Younger Dryas interval from thermally fractionated gases in polar ice. *Nature*, *391*(6663), 141-146.

Shackleton, N.J., Hall, M.A., Vincent, E., 2000. Phase relationships between millennial-scale events 64,000–24,000 years ago. Paleoceanography 15, 565–569.

Shen, C.-C., Wu, C.-C., Cheng, H., Edwards, R.L., Hsieh, Y.-T., Gallet, S., Chang, C.-C., Li, T.-Y., Lam, D.D., Kano, A., 2012. High-precision and high-resolution carbonate 230Th dating by MC-ICP-MS with SEM protocols. Geochim. Cosmochim. Acta 99, 71–86.

Sirocko, F., Knapp, H., Dreher, F., Förster, M.W., Albert, J., Brunck, H., Veres, D., Dietrich, S., Zech, M., Hambach, U., Röhner, M., Rudert, S., Schwibus, K., Adams, C., Sigl, P., 2016. The ELSA-Vegetation-Stack: Reconstruction of Landscape Evolution Zones (LEZ) from laminated Eifel maar sediments of the last 60,000 years. Glob. Planet. Change 142, 108–135. https://doi.org/10.1016/j.gloplacha.2016.03.005

Smith, F.H., Janković, I., Karavanić, I., 2005. The assimilation model, modern human origins in

Europe, and the extinction of Neandertals. Quat. Int. 137, 7–19.

Spötl, C., & Mangini, A. (2002). Stalagmite from the Austrian Alps reveals Dansgaard–Oeschger events during isotope stage 3:: Implications for the absolute chronology of Greenland ice cores. *Earth and Planetary Science Letters*, *203*(1), 507-518.

Spötl, C., Mangini, A., Richards, D.A., 2006. Chronology and paleoenvironment of Marine Isotope Stage 3 from two high-elevation speleothems, Austrian Alps. Quat. Sci. Rev. 25, 1127–1136. https://doi.org/10.1016/j.quascirev.2005.10.006

Staubwasser, M., Drăgușin, V., Onac, B.P., Assonov, S., Ersek, V., Hoffmann, D.L., Veres, D., 2018. Impact of climate change on the transition of Neanderthals to modern humans in Europe. Proc. Natl. Acad. Sci. 115, 9116–9121.

Svensson, A., Andersen, K.K., Bigler, M., Clausen, H.B., Dahl-Jensen, D., Davies, S.M., Johnsen, S.J., Muscheler, R., Parrenin, F., Rasmussen, S.O., 2008. A 60 000 year Greenland stratigraphic ice core chronology. Clim. Past 4, 47–57.

Talamo, S., Aldeias, V., Goldberg, P., Chiotti, L., Dibble, H.L., Guérin, G., Hublin, J., Madelaine, S., Maria, R., Sandgathe, D., 2020. The new 14C chronology for the Palaeolithic site of La Ferrassie, France: the disappearance of Neanderthals and the arrival of Homo sapiens in France. J. Quat. Sci. 35, 961–973.

Timmermann, A., 2020. Quantifying the potential causes of Neanderthal extinction: Abrupt climate change versus competition and interbreeding. Quat. Sci. Rev. 238, 106331.

Treble, P., Shelley, J. M. G., & Chappell, J. 2003. Comparison of high resolution sub-annual records of trace elements in a modern (1911–1992) speleothem with instrumental climate data from southwest Australia. *Earth and Planetary Science Letters*, *216*(1-2), 141-153.

Tremaine, D. M., Froelich, P. N., & Wang, Y. 2011. Speleothem calcite farmed in situ: Modern calibration of δ18O and δ13C paleoclimate proxies in a continuously-monitored natural cave system. *Geochimica et Cosmochimica Acta*, *75*(17), 4929-4950.

Van Kreveld, S., Sarnthein, M., Erlenkeuser, H., Grootes, P., Jung, S., Nadeau, M. J., ... & Voelker, A. 2000. Potential links between surging ice sheets, circulation changes, and the Dansgaard-Oeschger cycles in the Irminger Sea, 60–18 kyr. *Paleoceanography*, *15*(4), 425-442.

Van Rampelbergh, M., Verheyden, S., Allan, M., Quinif, Y., Keppens, E., & Claeys, P. (2014). Monitoring of a fast-growing speleothem site from the Han-sur-Lesse cave, Belgium, indicates equilibrium deposition of the seasonal δ 18 O and δ 13 C signals in the calcite. *Climate of the Past*, *10*(5), 1871-1885.

Van Rampelbergh, M., Verheyden, S., Allan, M., Quinif, Y., Cheng, H., Edwards, L. R., ... & Claeys, P. (2015). A 500-year seasonally resolved δ 18 O and δ 13 C, layer thickness and calcite aspect record from a speleothem deposited in the Han-sur-Lesse cave, Belgium. *Climate of the Past*, *11*(6), 789-802.

Vansteenberge, S., Verheyden, S., Genty, D., Blamart, D., Goderis, S., Van Malderen, S. J., ... & Claeys, P. (2019). Characterizing the Eemian-Weichselian transition in northwestern Europe with three multiproxy speleothem archives from the Belgian Han-sur-Lesse and Remouchamps cave systems. *Quaternary Science Reviews*, *208*, 21-37.

Vansteenberge, S., De Winter, N.J., Sinnesael, M., Verheyden, S., Goderis, S., Van Malderen, S.J.M., Vanhaecke, F., Claeys, P., 2020. Reconstructing seasonality through stable-isotope and trace-element analyses of the Proserpine stalagmite, Han-sur-Lesse cave, Belgium: indications for climate-driven changes during the last 400 years. Clim. Past 16, 141–160.

Verheyden, S., Keppens, E., Fairchild, I. J., McDermott, F., & Weis, D. (2000). Mg, Sr and Sr isotope geochemistry of a Belgian Holocene speleothem: implications for paleoclimate reconstructions. *Chemical Geology*, *169*(1-2), 131-144.

Verheyden, S., Baele, J. M., Keppens, E., Genty, D., Cattani, O., Cheng, H., ... & Quinif, Y. (2006). The Proserpine stalagmite (Han-Sur-Lesse Cave, Belgium): preliminary environmental interpretation of the last 1000 years as recorded in a layered speleothem. *Geologica Belgica*, *9*, 245-256.

Verheyden, S., Nader, F. H., Cheng, H. J., Edwards, L. R., & Swennen, R. (2008). Paleoclimate reconstruction in the Levant region from the geochemistry of a Holocene stalagmite from the Jeita cave, Lebanon. *Quaternary Research*, *70*(3), 368-381.

Verheyden, S., Keppens, E., Van Strydonck, M., & Quinif, Y. (2012). The 8.2 ka event: is it registered in Belgian speleothems?. *Speleogenesis & Evolution of Karst Aquifers*, (12).

Verheyden, S., Keppens, E., Quinif, Y., Cheng, H. J., & Edwards, L. R. (2014). Late-glacial and Holocene climate reconstruction as inferred from a stalagmite-Grotte du Pere Noel, Han-sur-Lesse, Belgium. *Geologica Belgica*.

Wainer, K., Genty, D., Blamart, D., Hoffmann, D., Couchoud, I., 2009. A new stage 3 millennial climatic variability record from a SW France speleothem. Palaeogeogr. Palaeoclimatol. Palaeoecol. 271, 130–139. https://doi.org/10.1016/j.palaeo.2008.10.009

Weber, M., Scholz, D., Schröder-Ritzrau, A., Deininger, M., Spötl, C., Lugli, F., Mertz-Kraus, R., Jochum, K.P., Fohlmeister, J., Stumpf, C.F., 2018. Evidence of warm and humid interstadials in central Europe during early MIS 3 revealed by a multi-proxy speleothem record. Quat. Sci. Rev. 200, 276–286.

Welker, F., Hajdinjak, M., Talamo, S., Jaouen, K., Dannemann, M., David, F., ... & Hublin, J. J. 2016. Palaeoproteomic evidence identifies archaic hominins associated with the Châtelperronian at the Grotte du Renne. *Proceedings of the National Academy of Sciences*, *113*(40), 11162-11167.

Acknowledgment

We thank Ari Lannoy, guide at the Han-sur-Lesse cave for monitoring the cave temperatures. We also thank David Verstraeten for his help in the lab. And we thank the 2 anonymous reviewers for their helpful comments, allowing us to significantly improve the manuscript. MP thanks VUB (OZR opvangmandaat' number 3772), IODP-France and Research Foundation – Flanders (FWO) (senior postdoctoral grant (208064 / 1255923N LV 4508) for their supports. TVA thanks FWO for his junior postdoctoral fellowship grant (FWO.3E0.2022.0048.01) and FV acknowledges the FWO-Vlaanderen for financial support under the form of research project G017217N. PhC and SG thank the VUB Strategic Program, and the Research Foundation Flanders (FWO) Hercules Program for the acquisition of the IRMS and µXRF instruments used in this study. TF thanks the support of University of Bordeaux's IdEX "Investments for the Future" program / GPR "Human Past" (postdoctoral grant).

Supplementary material

A new insight of the MIS 3 Dansgaard-Oeschger climate oscillations in western Europe from the study of a Belgium isotopically equilibrated speleothem

M. Peral[1,2*], M. Marchegiano[1,3], S. Verheyden[4], S. Goderis[1], T. Van Helden[5], F. Vanhaecke[5], T. Van Acker[5], T. Dehais[1], X. Jia[6], H. Cheng[6], J. Fiebig[7], T. Fourcade[2,8], C. Snoeck[1,9], Ph. Claeys[1]

1. Archaeology, Environmental changes & Geo-Chemistry, Vrije Universiteit Brussel, Belgium
2. Environnements et Paléoenvironnements Océaniques et Continentaux (EPOC), UMR CNRS 5805, Université de Bordeaux, 33600 Pessac, France
3. Departamento de Estratigrafía y Paleontología, Universidad de Granada, 18071 Granada, España
4. Royal Belgian Institute for Natural Sciences (RBINS), Belgium
5. Atomic & Mass Spectrometry – A&MS Research Group, Department of Chemistry, Ghent University, Campus Sterre, Krijgslaan 281-S12, 9000 Ghent, Belgium
6. Institute of Global Environmental Change, Xi'an Jiaotong University, China
7. Institut für Geowissenschaften, Goethe Universität, Altenhöferallee 1, 60438 Frankfurt am Main, Germany
8. Archéosciences Bordeaux, UMR 6034, Université Bordeaux Montaigne, CNRS, Maison de l'Archéologie, Esplanade des Antilles, 33600 Pessac, France
9. Multidisciplinary Archaeological Research Institute, Vrije Universiteit Brussel, Belgium

* marion.peral@vub.be or marion.peral@u-bordeaux.fr

Discussion age model:

In the manuscript, we apply a linear age model, including all dating in a single fit, performed using StalAge. The limitation of this age model is the loss of potential changes in the deposition rate. To check the impact of the deposition rate, we also calculated an age model assuming a constant deposition rate between two neighboring dates only, using the OxCal V4.4 Bronk Ramsey (2021). As discussed by Scholz et al. (2012), both StalAge and OxCal can be used to create an age model from U/Th dating in speleothems. Figure S1 shows the age model recalculated with linear fits only between 2 neighboring dates, using the OxCal software.

The effects of two age models on the isotopic measurements are compared in Figure S2. The black color corresponds to the age model made using StalAge, while the orange color corresponds to the age model made using OxCal. There are no significant changes between the two age models, except between 48 and 47 ka (Fig. 2). During this period, the OxCal age model places the warmest temperature derived from the clumped isotope, associated with the most negative $\delta^{18}O$ peak, during the H5 event, which is expected to be cold. This model can thus be considered highly unlikely. For this reason, we used the StalAge age model, placing the warmest temperature at the end of H5 and the start of DO-12. The two dates of samples 6 and 7, corresponding to DO-13 as defined in the literature, were sampled deeper in the stratigraphy compared to the clumped isotope measurement recording the warmest temperature. This therefore implies that the recorded high temperature is probably not associated with DO-13 but more likely with DO-12.

Slow growing speleothems, precipitated close to the isotopic equilibrium, are often not used in paleoclimatology because they are rare and because of their low resolutions (Daëron et al., 2019; Wassenburg et al., 2021). As a result the limitation of our age model can be due to the use of a slow growing speleothem, making it difficult to identify potential changes in deposition rates due to the low temporal resolution. Age model programs are maybe not well suited for these unusual speleothems.

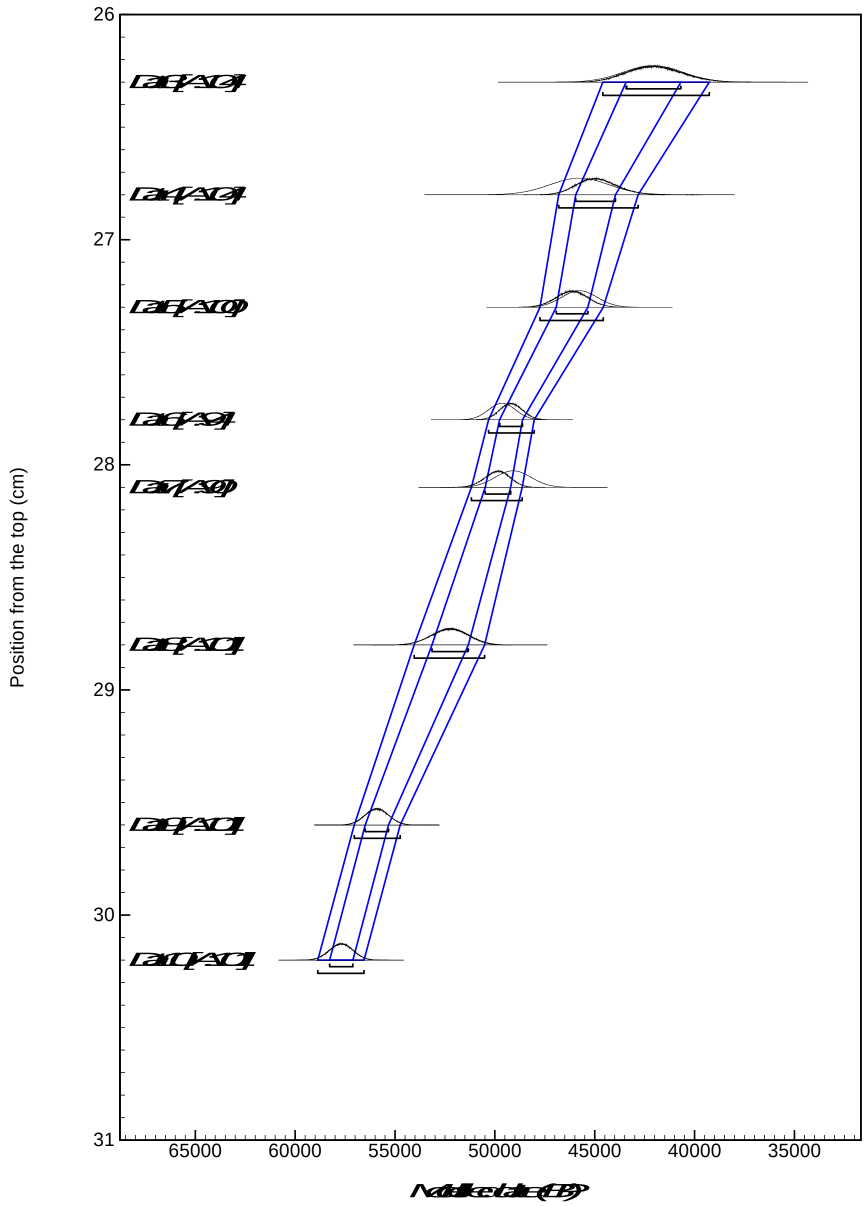

Figure S1: Age model performed using OxCal. The sampling uncertainties are used. Dark blue corresponds to the 68.3% uncertainties and light blue to 95.4% uncertainties.

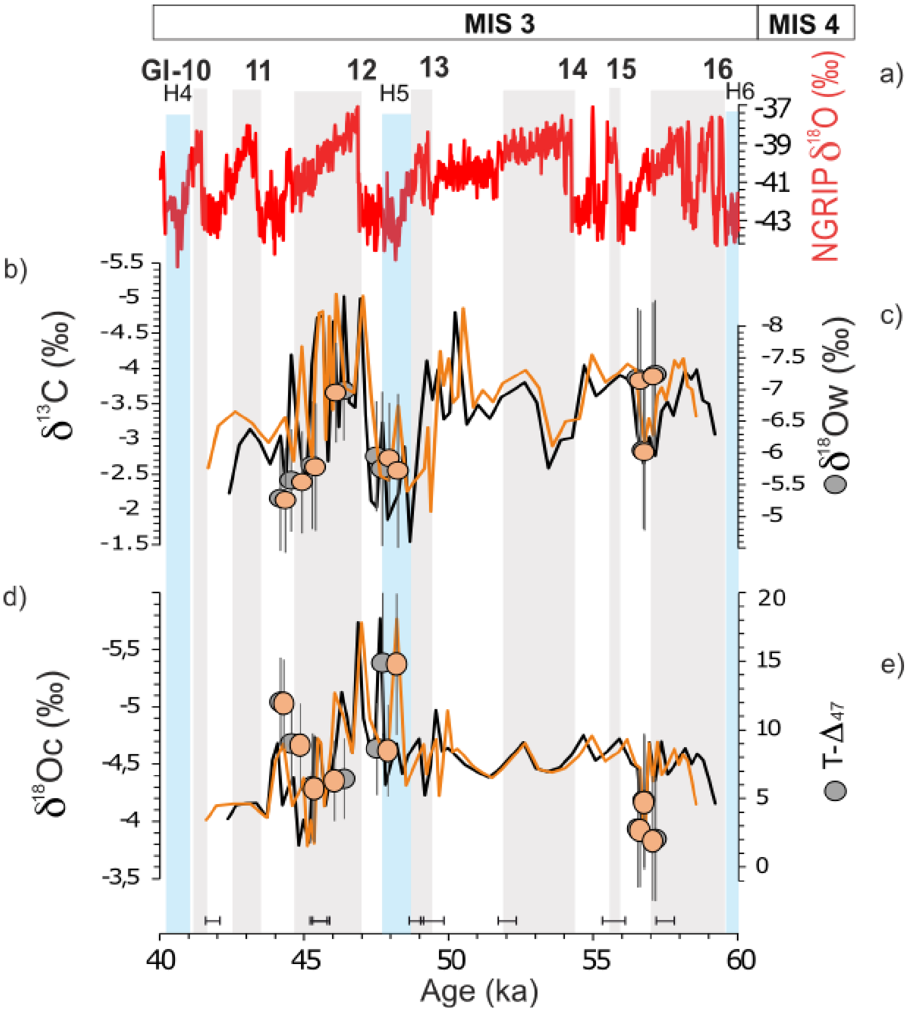

Figure S2: Comparison between the effects of the two age models on the isotopic measurements. The NGRIP $\delta^{18}O$ (a) is compared to isotopic measurements of I-B2: $\delta^{13}C$ curve (b) with $\delta^{18}O$ of the water (c) and $\delta^{18}O$ curve (d) with clumped isotope derived temperatures (e). The obtained dates are also represented at the bottom of the plot. The uncertainties are at 2SE. The black data correspond to the age model from StalAge. The orange data correspond to the age model from OxCal.

Table S1: summary of the Incomparable speleothem dating. The orange columns are the dating using for the age model with associated uncertainties resulting of the sampling uncertainties.

Sample Dat-	^{238}U *(ppb)*		^{232}Th *(ppt)*		^{230}Th / ^{232}Th *(atomic x10-6)*		$\delta^{234}U$* *(measured)*		^{230}Th / ^{238}U *(activity)*		^{230}Th Age *(uncorrected)*		^{230}Th Age *(corrected)*		$\delta^{234}U_{Initial}$** *(corrected)*		^{230}Th Age (BP)*** *(corrected)*		Depth		Final age SE
Interval-B1		SE		SE		SE		SE		SE	ka	SE	ka	SE		SE	ka	SE	cm	SE	ka
1	177.1	0.3	1733	±35	488	±10	1820	±3	0.2896	0.0007	11.6850	±0.0003	11.5860	±0.076	1881	±3	11.5170	±0.076	25.6	0.2	-
Interval-B2																					
2	116.1	0.2	962	±19	1611	±33	1714	±3	0.8099	0.0019	37.2080	±0.0113	37.1247	±0.127	1903	±4	37.0528	±0.127	25.7	0.2	-
3	86.3	0.1	477	±10	2578	±52	1608	±3	0.8656	0.0017	42.1380	±0.0118	42.0810	±0.124	1810	±4	42.0810	±0.124	26.3	0.2	1.473
4	77.1	0.1	259	±5	4482	±92	1565	±3	0.9145	0.0026	45.8752	±0.0168	45.8244	±0.170	1781	±4	45.7634	±0.170	26.8	0.2	1.473
5	91,0	0.1	355	±7	3872	±78	1574	±3	0.9181	0.0019	45.8746	±0.0124	45.8339	±0.127	1792	±3	45.7673	±0.127	27.3	0.2	0.883
6	55.9	0.1	318	±6	2745	±56	1486	±3	0.9482	0.0029	49.7763	±0.0198	49.7151	±0.203	1710	±4	49.6431	±0.203	27.8	0.2	0.671
7	73.6	0.1	391	±8	2837	±57	1421	±2	0.914	0.0016	49.2180	±0.0118	49.1592	±0.125	1632	±3	49.0882	±0.125	28.1	0.2	0.898
8	77.7	0.1	521	±10	2438	±49	1493	±3	0.9915	0.0019	52.3724	±0.0145	52.3018	±0.154	1731	±4	52.2308	±0.154	28.8	0.2	0.921
9	104.9	0.1	1506	±30	1219	±25	1522	±3	1.0616	0.0021	56.1374	±0.0165	55.9871	±0.196	1783	±4	55.9161	±0.196	29.6	0.2	0.593
10	113.4	0.1	914	±18	2248	±45	1548	±3	1.0991	0.0019	57.8470	±0.0147	57.7640	±0.158	1822	±3	57.6950	±0.158	30.2	0.2	0.593
Interval-B3																					
11	57.6	0.1	934	±19	1032	±21	912	±3	1.0151	0.0023	76.9050	±0.0277	76.6840	±0.317	1133	±3	76.6150	±0.317	30.9	0.2	-

U decay constants: l_{238} = 1.55125x10^{-10} (Jaffey et al., 1971) and l_{234} = 2.82206x10^{-6} (Cheng et al., 2013). Th decay constant: l_{230} = 9.1705x10^{-6} (Cheng et al., 2013).
*$\delta^{234}U$ = ([^{234}U/^{238}U]activity – 1)x1000.
** $\delta^{234}U_{initial}$ was calculated based on ^{230Th} age (T), i.e., $\delta^{234}U_{initial}$ = $\delta^{234}U_{measured}$ x e(l_{234} x T). Corrected ^{230}Th ages assume the initial $^{230}Th/^{232}Th$ atomic ratio of 4.4 ±2.2 x 10^{-6}. Those are the values for a material at secular equilibrium, with the bulk earth $^{232}Th/^{238}U$ value of 3.8. The errors are arbitrarily assumed to be 50%.
***B.P. stands for “Before Present” where the “Present” is defined as the year 1950 A.D.

Table S2: Bulk oxygen and carbon isotope results
See CSV file, named "bulk-results"

Table S3: Overview of the nuclides selected for monitoring and the corresponding dwell times.

Element	**m/Z Q1 and Q2**	**Dwell time (ms)**
Mg	25	50
Al	27	25
P	31	50
Ca	43	100
Fe	57	50
Zn	66	100
Sr	88	50
Y	89	125
Ba	137	100
Pb	208	100
Th	232	100
U	238	100
Total scan cycle time		**995.2**

Table S4: Trace element results from LA-ICP-MS
See XLS file, named "element-results"

Table S5: Clumped-isotope results
See XLS file, named "clumped-results"

Table S6: Dual clumped isotope results
See XLS file, named "dual-clumped-results"

Table S7: Remodeled chronology of Ormesson Châtelperronian site (ages in years BP and uncertainties at 95% interval).

Ormesson (seine et Marne) (Bodu et al., 2017)	ages uncertainties 95% interval (years BP)	
End	40336	36328
Châtelperronian	46305	35842
Begin	45975	41631

Figures S1 to S4 represent the μXRF maps of Al, K, Fe and Si element content at high resolution.

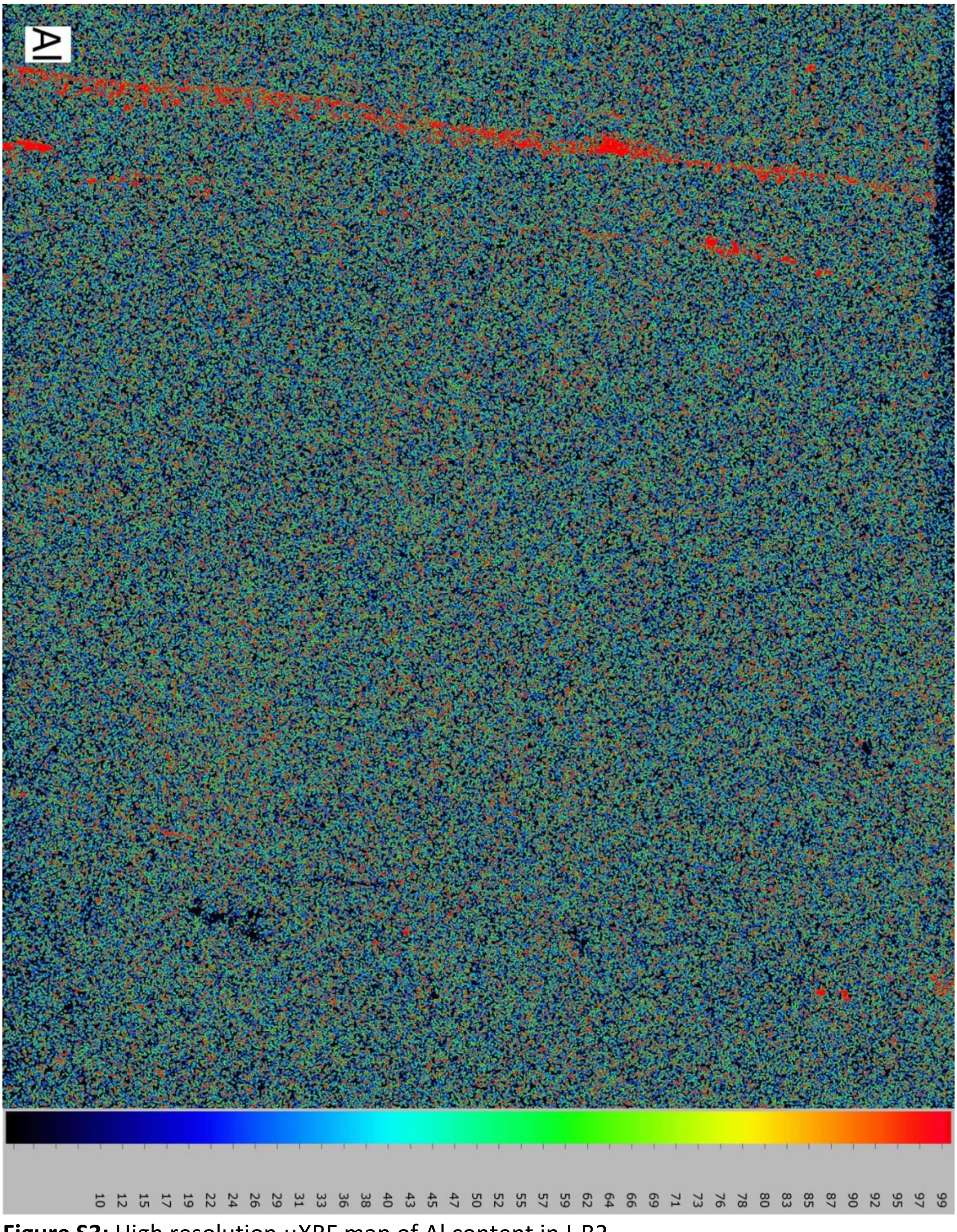

Figure S3: High resolution μXRF map of Al content in I-B2

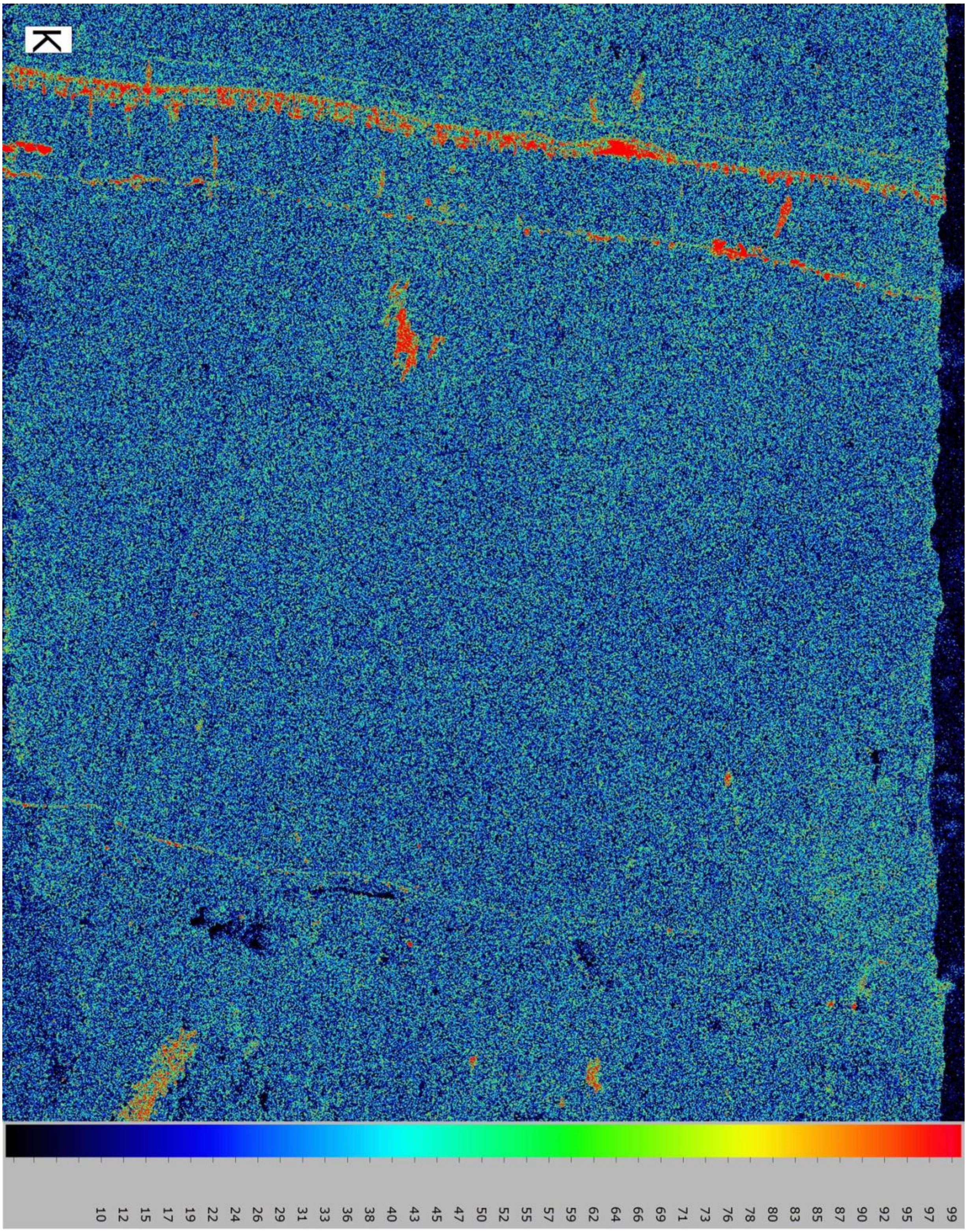

Figure S4: High resolution μXRF map of K content in I-B2

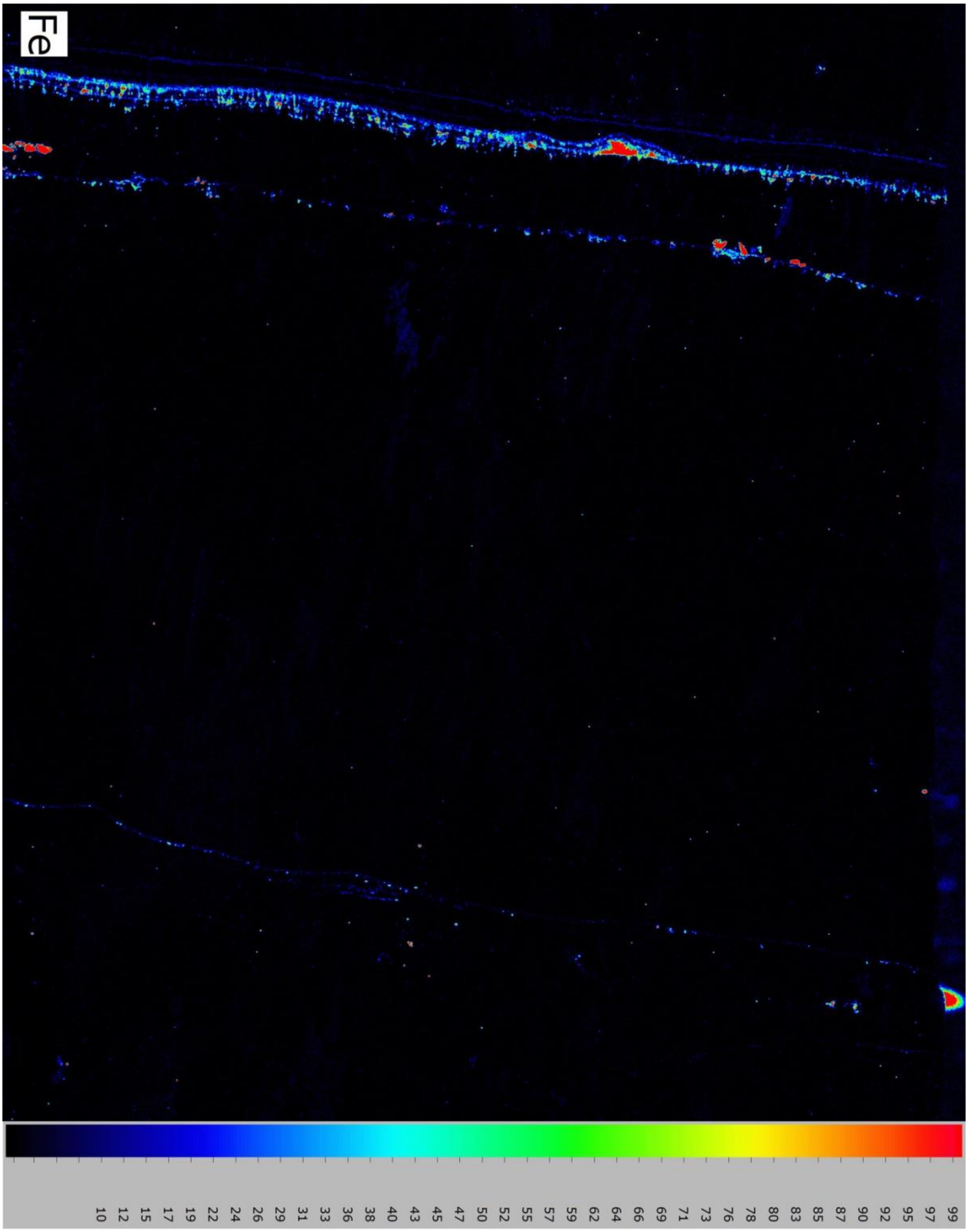

Figure S5: High resolution μXRF map of Fe content in I-B2

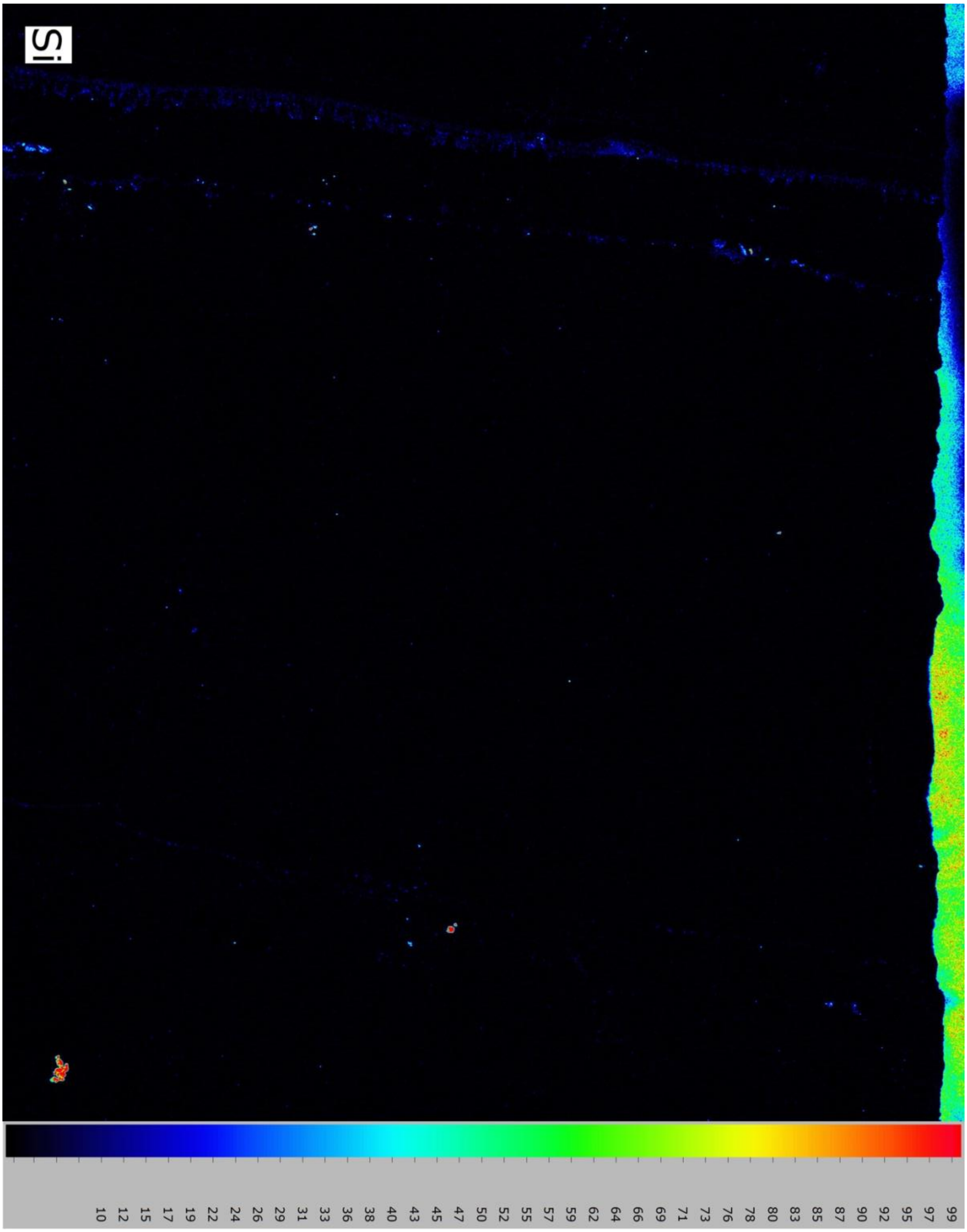

Figure S6: High resolution μXRF map of Si content in I-B2

References:

Daëron, M., Drysdale, R.N., Peral, M., Huyghe, D., Blamart, D., Coplen, T.B., Lartaud, F., Zanchetta, G., 2019. Most Earth-surface calcites precipitate out of isotopic equilibrium. Nat. Commun. https://doi.org/10.1038/s41467-019-08336-5

Scholz, D., Hoffmann, D. L., Hellstrom, J., & Ramsey, C. B. (2012). A comparison of different methods for speleothem age modelling. *Quaternary Geochronology*, *14*, 94-104.

Wassenburg, J. A., Vonhof, H. B., Cheng, H., Martínez-García, A., Ebner, P. R., Li, X., ... & Haug, G. H. (2021). Penultimate deglaciation Asian monsoon response to North Atlantic circulation collapse. *Nature Geoscience*, *14*(12), 937-941.